DEVELOPMENT OF FISSION SUPPRESSION DEVICES FOR AFRODITE

Thulani Thokozani Hlatshwayo

Thesis submitted in fulfillment of the requirements

for the degree of Master of Sciences

in the Department of Physics and Engineering

University of Zululand.

Supervisors

Supervisor: Dr. R.A. Bark

Co-supervisor: Prof. O.M. Ndwandwe

December 2005

DECLARATION

I, the undersigned, hereby declare that the work contained in this thesis is my own original work and that I have not previously in its entirety or in part submitted it at any university for a degree.

Signature: ....

Date: ....

ABSTRACT

The discovery of the third minimum in various heavy mass nuclei, for example, in the U-Th region, has developed interest in the nuclear physics community to study the behaviour of the nucleus in this minimum. The nuclear shape that is predicted to exist in this minimum is known as a hyperdeformed shape, which corresponds to 3:1 major to minor axis ratio. A hyperdeformed nucleus could be created when a heavy target is bombarded with a light beam, for example, when an α-particle beam bombards ^{232}Th. However in such a reaction, the strongest channel is fission, which occurs almost 99% of the time. Due to the high fission background, which reduces the experimental sensitivity for picking out γ decay of hyperdeformed states from the background, many experiments have failed to observe hyperdeformed bands in this minimum. Therefore, this thesis focuses on the development of two fission suppression devices, namely a recoil detector and a solar cell array at iThemba LABS (South Africa).

ACKNOWLEDGEMENTS

I wish to express my sincere gratitude to the following people for making this project successful, ngaphandle kwenu angilutho mina.

- My Mighty God and my ancestors for giving me strength to go from nowhere to where I am today;
- My research supervisor Dr. R.A. Bark for guidance and patience that he gave me throughout this project;
- Prof O.M. Ndwandwe my University supervisor for the support that he gave me;
- Dr. S.M. Mullins for his invaluable help and increasing the flow of the thesis by proof reading it;
- Dr. J.J. Lawrie for allowing me to pursue this research in Physics Group;
- All iThemba LABS Physics group for their assistance they gave me;
- The NRF and iThemba LABS for the funding I received.
- The MANUS, MATSCi, and all postgraduates students for their spiritual support that they gave me;
- Sean Murray and his colleagues for their assistance whenever I had computer related problems;
- Radio Isotopes group for allowing me to use their lab for mounting foils;
- All those who assisted during weekends of data acquisition;
- Nozipho Zungu (My wife to be) and Asanda (my son) for their understanding;
- Lastly, I like to thank all my family especially my mother for their support that they gave me through this years, ngithi kini enikwenze kimi nikwenze nakwabanye ngiyabonga kakhulu.

This work is dedicated to the late, friend, father and the coordinator of MANUS and MATSCi projects Dr. T.K. Marais.

TABLE OF CONTENTS

LIST OF FIGURES

LIST OF TABLES

CHAPTER 1 INTRODUCTION

1.1 Background

This work is motivated by the desire to observe atomic nuclei under extreme conditions where they could be forced to take on exotic shapes. Mathematically, the different shapes of the nuclei are often described by a multipole series, such as an expansion in spherical harmonics $\mathrm{Y}(\theta,\phi)$:

$$R(\theta,\phi)=R_0\left[1+\sum_{\lambda=0}^{\infty}\sum_{\mu=-\lambda}^{\lambda}\alpha_{\lambda\mu}\mathrm{Y}_{\lambda\mu}(\theta,\phi)\right] \qquad 1.1$$

where R_0 is the radius of a spherical nucleus of equivalent volume and R is the radius vector. The shapes corresponding to different multipoles λ are shown in figure 1.1. The first important shape corresponds to quadrupole distortions with λ=2, while λ=3 corresponds to an octupole deformation and λ=4 to a hexadecapole deformation as shown in figure 1.1.

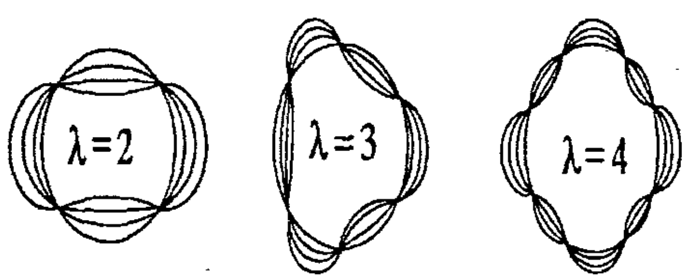

Figure 1-1: The shapes corresponding to the multipole deformations for λ=1, λ=2, λ=3, λ=4. Taken from [Mab03].

The distortion of the nucleus also affects the single particle energies of the constituent protons and neutrons. For example, if a harmonic oscillator is used as a nuclear potential, the resulting single particle energies as a function of the quadrupole deformation parameter ε_2 are shown in figure 1.2. The large shell gaps that are observed for particular nucleon numbers are associated with extra stability and predict Magic numbers [Wad02]. The harmonic oscillator must be modified to better mimic the nuclear potential e.g. by adding a spin orbit term in order to reproduce the spherical Magic numbers (2, 8, 20, 28, 50, 82, etc), which are known to lead to stable configurations. Nevertheless it can be seen in figure 1.2 that the pure harmonic oscillator predicts other shell gaps in the more ellipsoidal deformed shapes, beside the spherical nuclear shapes, at ratios of major to minor axis of 3:2, 2:1, or even 3:1. These ratios are known with some specific names. For example, 3:2 with ε_2=0.4 is known as highly deformed, 2:1 with ε_2=0.6 is known as the superdeformed (SD) shape and 3:1 with ε_2= 0.85 is known as the hyperdeformed (HD) shape.

The energy levels of the modified harmonic oscillator or Wood Saxon potential can be used in realistic calculations of potential energy, as a function of deformation, for a particular nucleus. For example, a potential energy surface as a function of quadrupole deformation, typical of the U-Th region, is shown in figure 1.3. Three different minima are calculated, which correspond to the shapes shown at the top of the figure. The first minimum corresponds to the normal deformed shape (ND), second minimum corresponds to the superdeformed shape (SD) and the third minimum corresponds to the hyperdeformed shape (HD). The third minimum is no longer reflection symmetric. In fact an octupole shape is predicted with $\beta_3 = \varepsilon_3 = 0.3$ as above the sketch of the hyperdeformed shape of the top of figure 1.3.

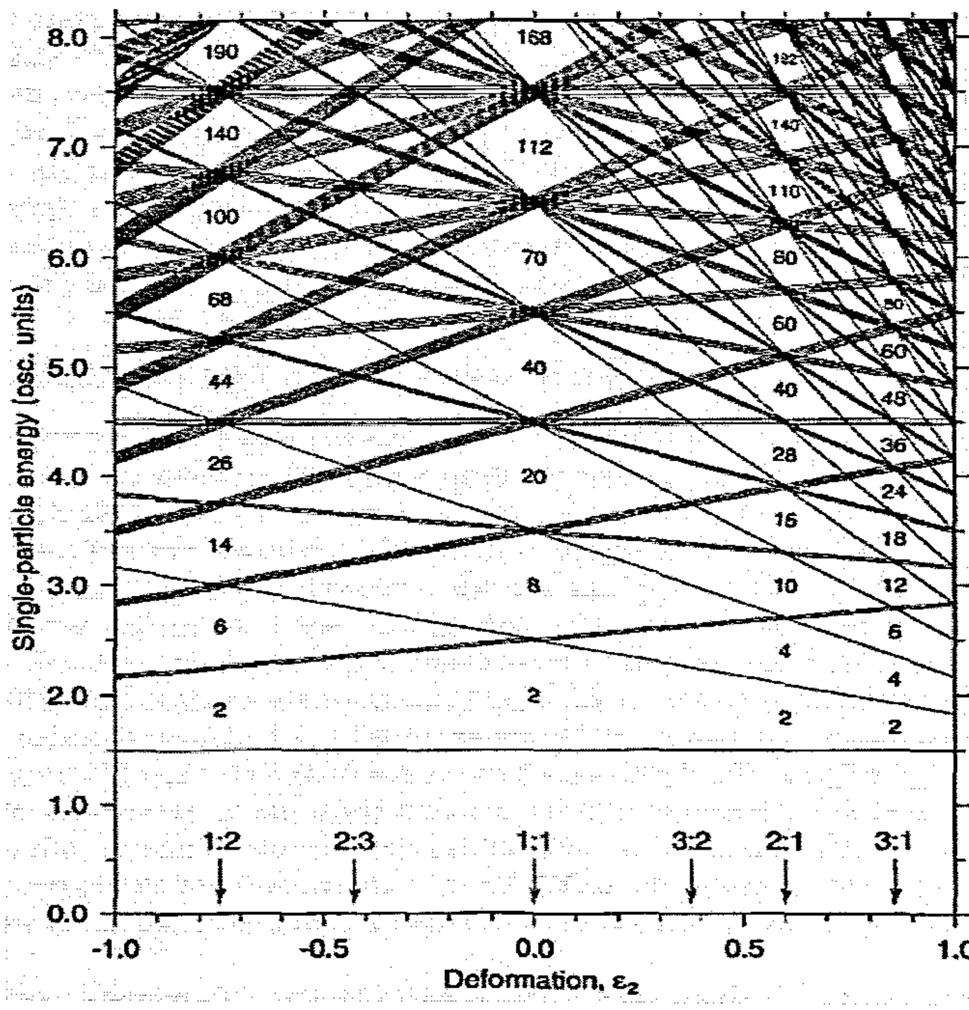

Figure 1-2: Harmonic oscillator energy levels as a function of deformation parameter ε_2. The large shell gaps for both prolate and oblate shapes are marked with numbers. The arrows on the bottom of the figure indicate the positions of spherical (1:1), highly deformed (3:2), superdeformed (2:1), and hyperdeformed (3:1) nuclear shapes, taken from [Wad02].

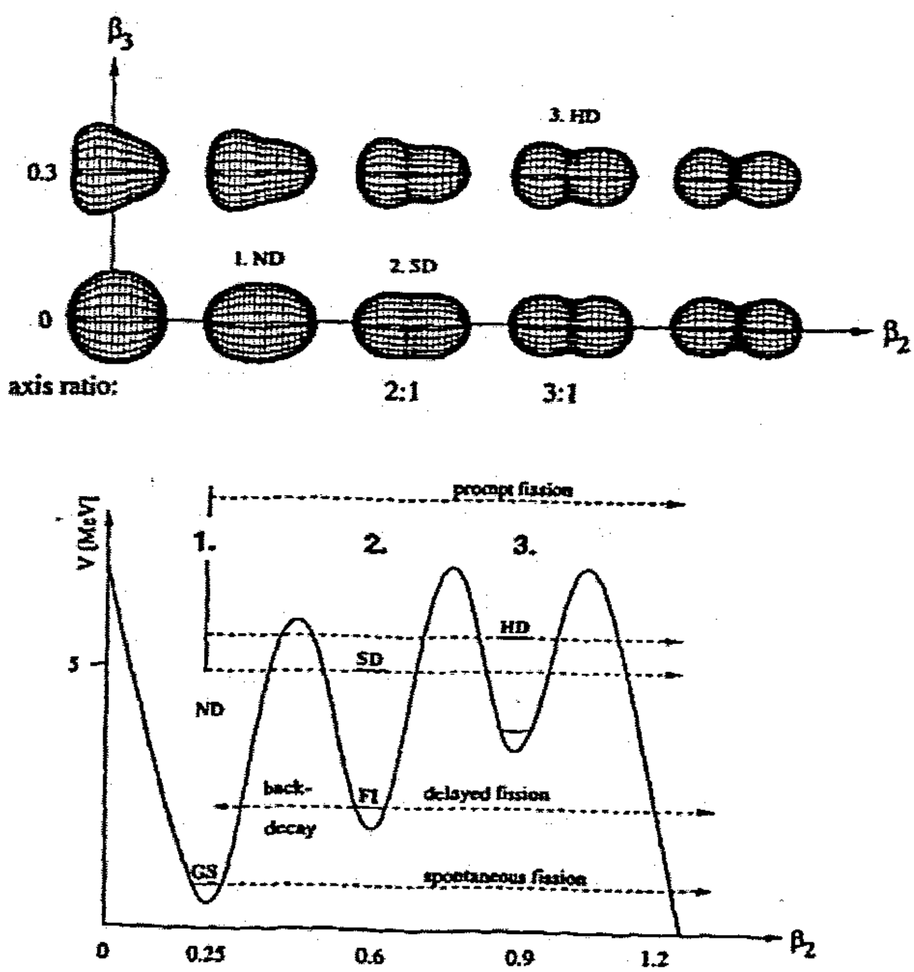

Figure 1-3. Lower part shows the plot of potential against quadrupole deformation, $\beta_2 \approx \varepsilon_2$, which reveals different minima for different shapes, and upper part, shows different, shapes that exist in different minima, taken from [Thi02].

Since the predicted deformed shapes break spherical symmetry, the nuclei are expected to be able be rotate about the axis perpendicular to their axis of symmetry. All the nucleons contribute to the rotation of nucleus, so that the rotation is called collective rotation and its energy is proportional to the square of the total angular momentum I.

$E = AI(I+1)$, where $A = \dfrac{\hbar^2}{2\Im}$ and $\Im$ is the nuclear moment of inertia.

If this rotational energy is calculated for different angular momentum or spin I, for example, I=0,2,4,6,etc, which are the allowed spins of the ground state band of even-even nuclei, a sequence of energy levels is predicted which is known as a rotational band. The levels in the rotational band with spin I preferentially decay to the next lowest level in the same band (having I-2) by emitting a γ- ray, until the band head is reached, typically within less than a few nanoseconds. The energies of these γ-rays are given by: $E_\gamma = A(4I-2)$ which is still proportional to the total angular momentum, and the difference in energy between two successive gamma rays is given by: $\Delta E_\gamma = \frac{4\hbar^2}{\Im} = 8A$.

Thus, a measurement of gamma-rays energies and spacing is related to the nuclear moment of inertia and therefore, deformation.

Excited nuclei at high spin can be created by the Heavy-Ion Fusion-Evaporation (HIFE) reaction, demonstrated in figure 1.4. When a projectile nucleus is accelerated to a kinetic energy that is more than the Coulomb barrier between itself and the target nucleus, the projectile can combine/fuse with the target and form the compound nucleus in an excited state. Depending on the energy of the projectile the compound nucleus is formed at high spin as shown in figure 1.5. The excited compound nucleus loses energy by fission or cooling down by emitting particles like neutrons (n), protons (p) or alphas (α). The emission of particles by the excited compound nucleus cools down the nucleus because the particles that are emitted take some portion of its energy [www1] [Bro81]. What remains is often called an evaporation residue. After that the nucleus cools down by emitting gamma rays until it reaches its ground state. The de-excitation by emitting gamma rays is categorized into statistical or cooling and discrete/slowing down emission. During the statistical emission a lot of energy is emitted and very little of angular momentum or spin is lost while in the discrete emission a large momentum is lost and smaller amount of energy is lost as shown in figure 1.5. The discrete emission follows a path close to the yrast line, the set of states with lowest energy for given spin, see figure 1.5.

Fission is a competing process where the compound nucleus splits into two fission fragments. The fission probability is higher in heavy compound nuclei. The instant where the heavy compound nucleus splits into two fragments is called scission point and those fragments that are formed are called primary fragments [Ahm95]. The primary fragments are formed in an excited state and cool down by neutron emission followed by gamma emission. The fragments, which no longer emit neutrons and finally lose their energy by emitting γ-rays are called secondary fragments. Secondary fission fragments, which cannot emit gamma rays, lose energy by beta decay.

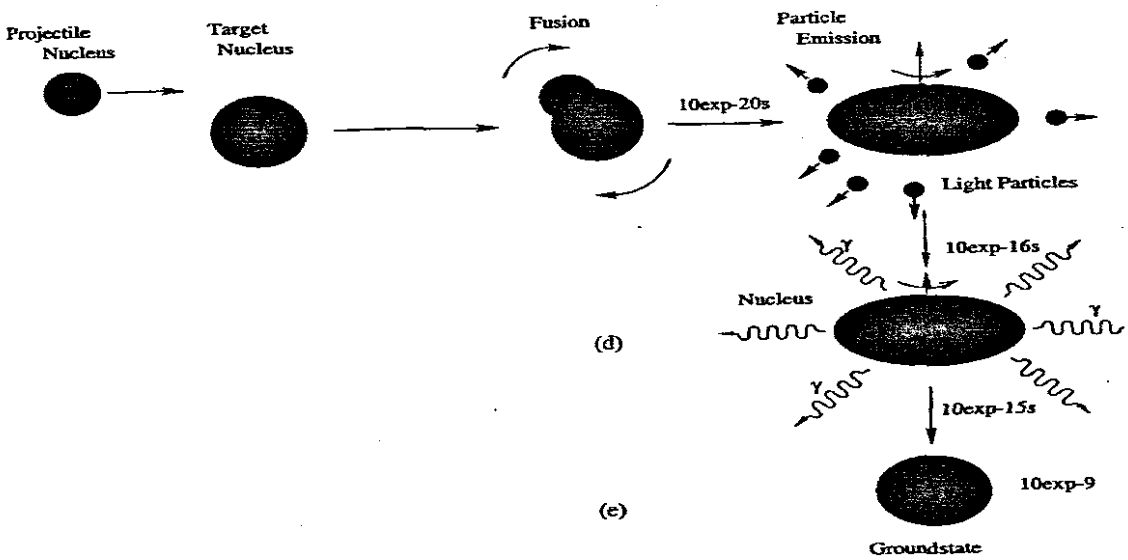

Figure 1-4: The schematic representation of a formation and decay sequence of an excited nucleus to an evaporation residue [Mab03].

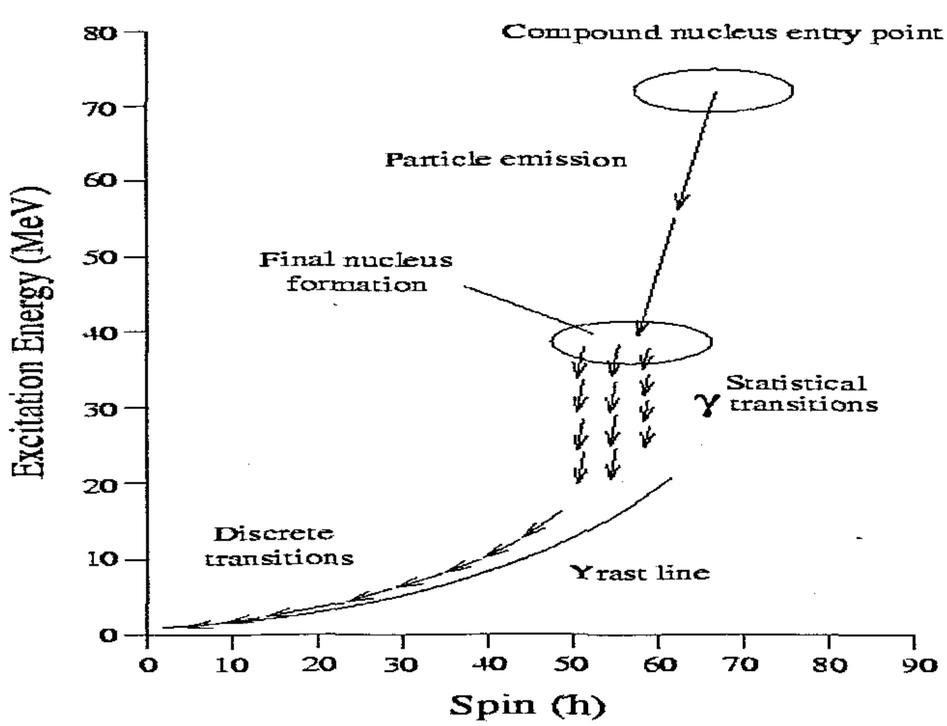

Figure 1-5: The illustration of how an excited compound nucleus is formed via Heavy-Ion Fusion-Evaporation reaction decays [www1].

In order to understand the properties of the excited states of the nuclei produced in the HIFE reactions, the γ-rays that are emitted can be detected and analyzed. Gamma rays are detected by High purity germanium (HPGe) detectors. For example, here at iThemba LABS, the detector array called AFRODITE is used for the detecting gamma rays. The AFRODITE array is combination of Clovers and LEPS detectors, described in detail in chapter 2.

Most gamma ray measurements are now performed in coincidence: that is at least two gamma rays are detected simultaneously. This improves the experimental sensitivity and allows different rotational bands of the nucleus to be isolated. A classical example of coincidence spectrum is shown in figure 1.6, where gamma rays from a superdeformed band were identified for the first time. Physicists have observed rotational bands in the first and second minima, but no gamma rays from third minimum have been observed yet, due to the competition from the strong fission channel encountered when attempting to make the hyperdeformed shape. In the hyperdeformed minimum the total energy is the sum of the rotational energy and the energy from the ground state to the third minimum i.e. $E = \frac{\hbar^2}{2\Im}\left(I(I+1)\right) + E_0$, where E_0 represents the excitation energy of the H.D (Hyperdeformed) band relative to the ground state.

The predicted hyperdeformed shape in the U-Th region is octupole (pear like) [Blo89] with reflection asymmetry as shown in figure 1.7, implying alternating parity band as shown in figure 1.8. The alternating parity levels are expected to be linked by E1 transitions. For these transitions, the gamma-ray energies are given by $E_\gamma = 2AI$. The value of A, inferred from measurements of fission resonances, and in agreement with calculations, is ~2 keV [Blo89]. Thus typical gamma-ray energies from the hyperdeformed band are expected to be between 40 and 120 keV between spins $10\hbar$ and $30\hbar$.

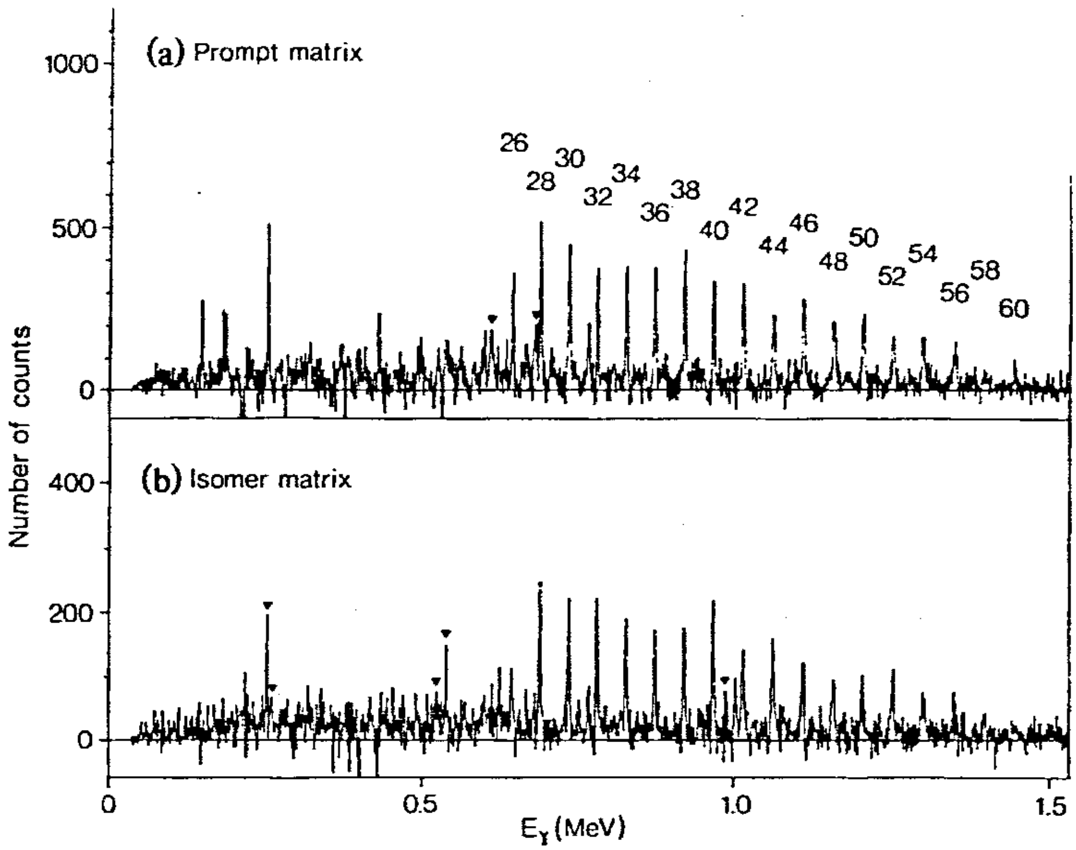

Figure 1-6: gamma-ray spectra in ^{152}Dy obtained by summation of gates set on the most members of superdeformed band [Twi89].

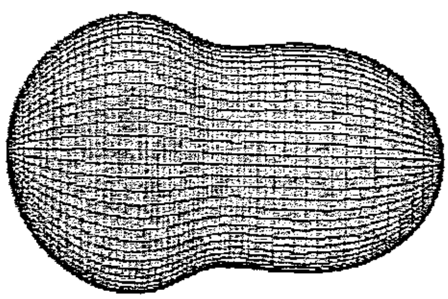

Figure 1-7: The octupole deformed nucleus.

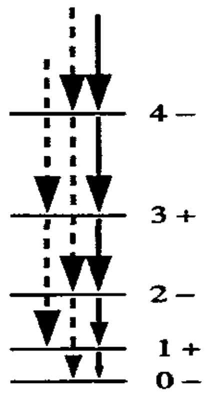

Figure 1-8: The example of an octupole band.

A hyperdeformed Uranium nucleus could be created by the following reaction:

$$^{232}\text{Th}\ (\alpha, 4n)\ ^{232}\text{U}.$$

Uranium-232 is the recoiling nucleus, which in this reaction, has a low recoil energy of about 1MeV, α is the alpha beam, ^{232}Th is the target, and 4n represents the neutrons that are released. The problem with detecting γ-rays from hyperdeformed nuclear states is that the production of the evaporation residue is in competition with fission [Cwi94], which can be described as:

$$^{232}\text{Th}\ (\alpha, xnf),$$

where f represents fission fragments, which are known to have kinetic energy of approximately 165 MeV and xn represents number of neutrons that are emitted. Fission in competition with the reaction of interest (forming ^{232}U) is dominant, accounting for almost 90% of the total fusion cross section, and that reduces the experimental sensitivity for picking out γ-rays from hyperdeformed states (from evaporation residues) from the background of fission. Due to this higher fission background, previous experiments have so far failed to observe discrete hyperdeformed gamma rays from the third minimum [Her03] [Haw99] [Hub05]. To pick up γ-rays from the evaporation residues, the fission background must be suppressed. The recoils in the first well are calculated to have 1to 10 mb range of cross section and in the second and third minimum they are calculated to have range < 1 μb [Lar69]. At the same time the AFRODITE is limited to 2mb, therefore this must be improved to μb range

1.2 Subject of the study

Two options for suppressing the fission background are considered here. The first option is to design a device that would be able to select and distinguish the evaporation residues from the background of fission products. A recoil detector is a device that detects the evaporation residues as they recoil out of the target. Many recoil detectors have already been built with various designs [Bec94][Lei95][Lei97], but the present recoil detector must be capable of detecting recoils with energies as low as 1 MeV, which would be produced in the ^{232}Th+α reaction and able to distinguish among ions so as to detect evaporation residues only.

The second option is to design the device that detects gamma rays in coincidence with fission fragments and then reject them i.e. act as fission veto. Since fission fragments are produced in every direction, the device suitable for detecting the fission fragments must cover a solid angle of 4π. Due to this requirement, a solar cell array has been developed to act as fission veto. Such a device could be useful in proton-induced reactions, where the recoil velocity would be insufficient to escape from any target of useful thickness and preclude the use of a recoil detector.

The hyperdeformed levels are predicted to decay with low gamma ray energies, which are well suited to be detected by the LEPS detectors in AFRODITE. If the fission suppression devices work, the spectrum expected for a hyperdeformed band is similar to the one shown in figure 1.6, which proved the existence of superdeformed band in ^{152}Dy [Twi86]. The difference expected from the spectrum of a hyperdeformed band is the spacing between successive γ-energies and the absolute magnitude of γ-energies. By the use of γ-γ measurements, that is where one gates on the specific gamma and then finds every gamma that is in coincidence with it, the hyperdeformed level scheme can be built.

The rest of this thesis is organized as follows:

Chapter 2 describes AFRODITE

Chapter 3 describes a recoil detector

Chapter 4 discusses a solar cell array

Chapter 5 discusses the experimental methods and equipments of a solar cell array test experiment.

Chapter 6 discusses the experimental setup of the solar cell Test experiment

Chapter 7 discusses results and data analyses

Chapter 8 contains summary and future studies

CHAPTER 2 AFRODITE

AFRODITE is an acronym derived from AFRican Omnipurpose Detector for Innovative Techniques and Experiments [New98]. The AFRODITE array is made up of two types of high purity germanium detector; namely low energy photon spectroscopy (LEPS) and Clover detectors. The detectors of AFRODITE are supported by an aluminium frame that has a rhombicuboctahedron shape with 18 square and 18 triangular facets. The two facets i.e. at 0° and 180° with respect to beam's path accommodate the beam pipe in a normal AFRODITE chamber i.e. the AFRODITE without the recoil detector. The other square facet of the AFRODITE at 90° with respect to the beam's direction is for used for target positioning system and the other 15 square are normally available for the mounting of detectors. Figure 2.1 shows part of AFRODITE support frame with mounted detectors (LEPS and clovers). In this figure detectors are mounted around the target chamber so as to detect gamma rays. A target ladder that moves vertically controls the target position inside the target chamber. The target ladder has three slots namely the target slots, empty slot and the slot for the ruby to focus the beam, therefore, by moving the ladder up and down the beam is focused by the ruby and then the target is put in place. A Compton-suppression shield that is made of bismuth germanate $Bi_4Ge_3O_{12}$ (BGO) is used to cover the clover detectors, which act as scintillators in gamma ray detection. The BGO Compton suppression shield is shown in figure 2.2.

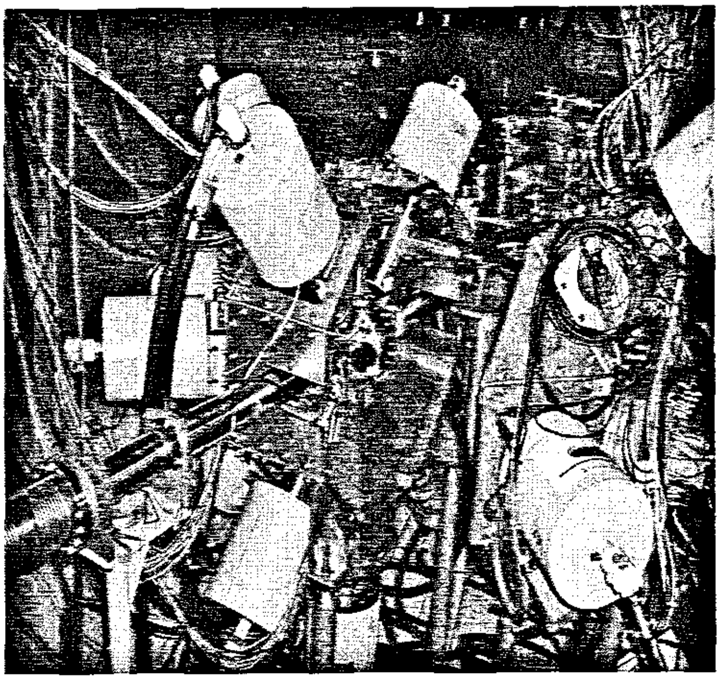

Figure 2-1: The part of AFRODITE with mounted gamma rays detectors (LEPS and clovers).

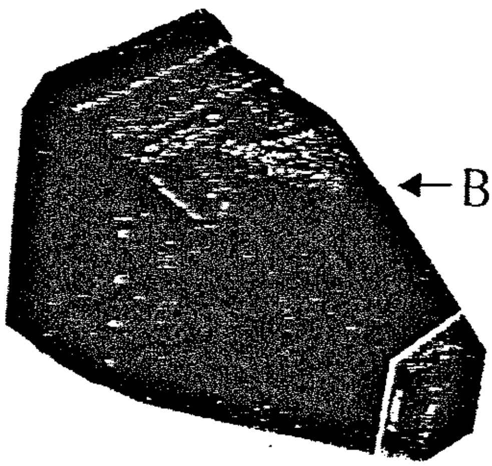

Figure 2-2: A BGO Compton suppression shield, showing the tapered heavy metal collimator with a 35 mm by 35-entrance window of gamma rays [Duc99].

2.1 Clover detectors

Clover detectors are made of four n-type coaxial HPGe crystal arranged in compact geometry and placed in a common crystal, these four n-type HPGe crystal are normally called elements of clover detectors, its geometric arrangement can be seen in figure 2.3. Each clover crystal element has its own preamplifier, thus allowing gamma rays detected by more than one element of the clover detector to be added. In order to reject the gamma rays Compton scattered out of the clover detector, they are always housed on bismuth germanate (BGO) suppression shield as shown in figure 2.4, (the one without BGO is shown in figure 2.5). For the BGO Suppressed clovers, the Compton scattered gamma rays from the germanium crystal are vetoed by the BGO shield while in the unsuppressed spectra from clover without BGO contains all gamma rays irrespective of whether they were scattered into BGO shields. Figure 2.6 shows two spectra, one from suppressed clovers (with BGO) and the other one from unsuppressed clovers (without BGO) measured using ^{137}Cs source [New98].

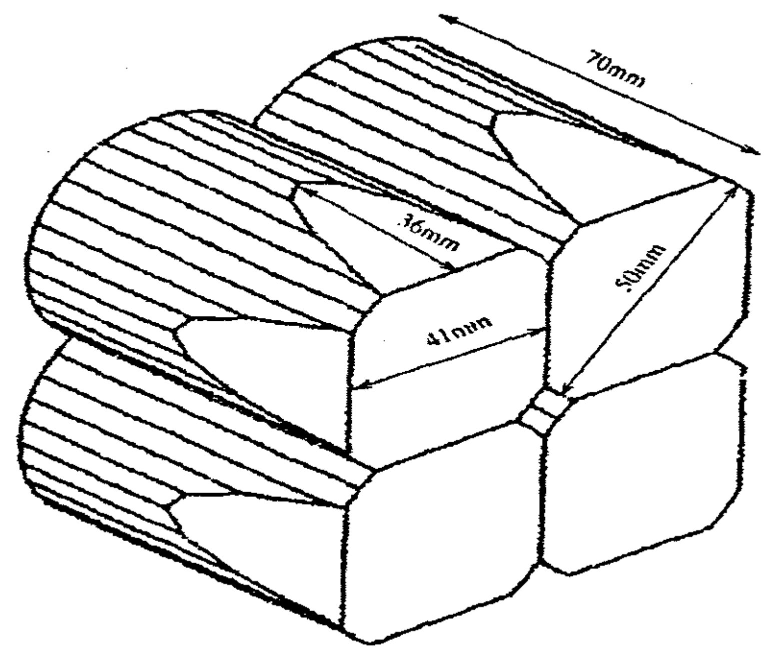

Figure 2-3: The arrangement of clover detectors elements [Jon95].

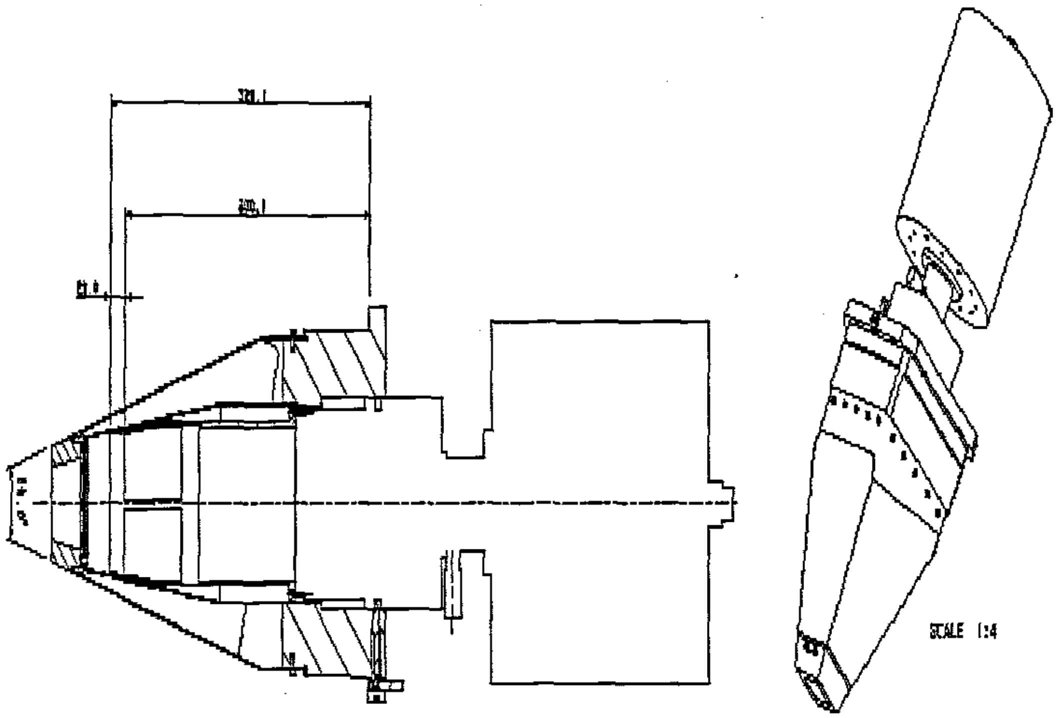

Figure 2-4: The schematic of a clover detector with BGO [www2].

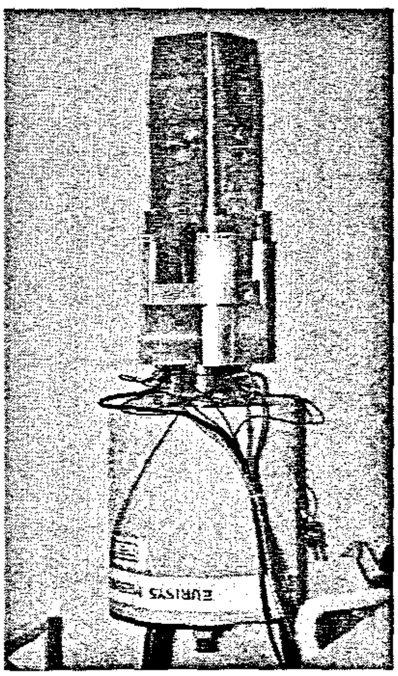

Figure 2-5: The clover detector without BGO.

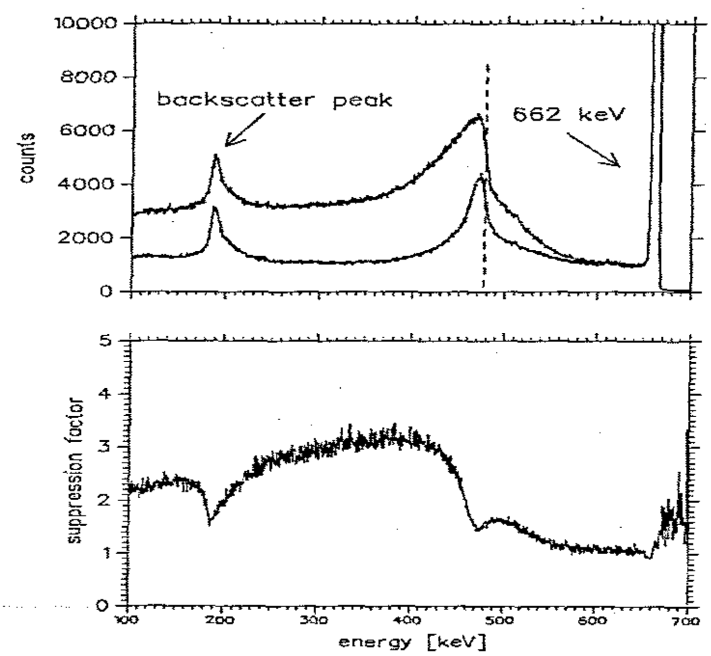

Figure 2-6: The top part of this figure shows the suppressed and unsuppressed spectra measured by placing ^{137}Cs source at the target position of the AFRODITE spectrometer (8 clovers, 7 LEPS), the Compton edge is shown by a dashed line. The bottom part shows the suppressed factors calculated from the data shown in the top part [New98].

2.2 LEPS detectors

LEPS detectors are made up of a single crystal of p-type HPGe with 10 mm of thickness and 60 mm of diameter and are electrically segmented into four quadrants. The LEPS detectors are more suitable for detection of low energy gamma rays due to their high relative efficiency at low energy (30 – 300 keV). The LEPS detector Dewars are filled with liquid nitrogen (LN_2) every 24 hours. The picture of a LEPS detector is shown in figure 4.7. The efficiency of 7 Clovers and 8 LEPS detectors is shown in figure 2.8 as measured by [New98] using ^{152}Eu and ^{133}Ba radioactive sources.

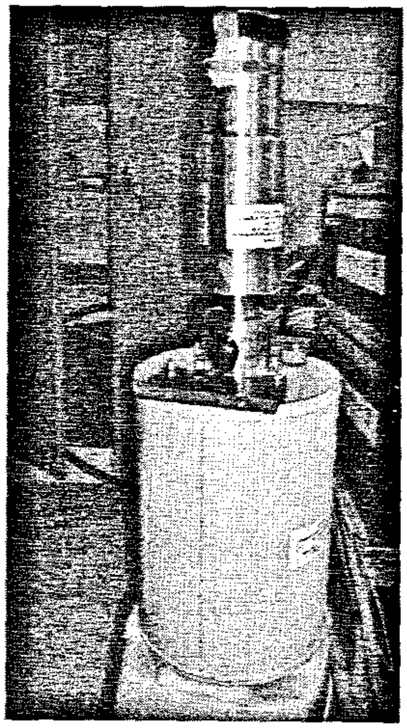

Figure 2-7: The LEPS detector.

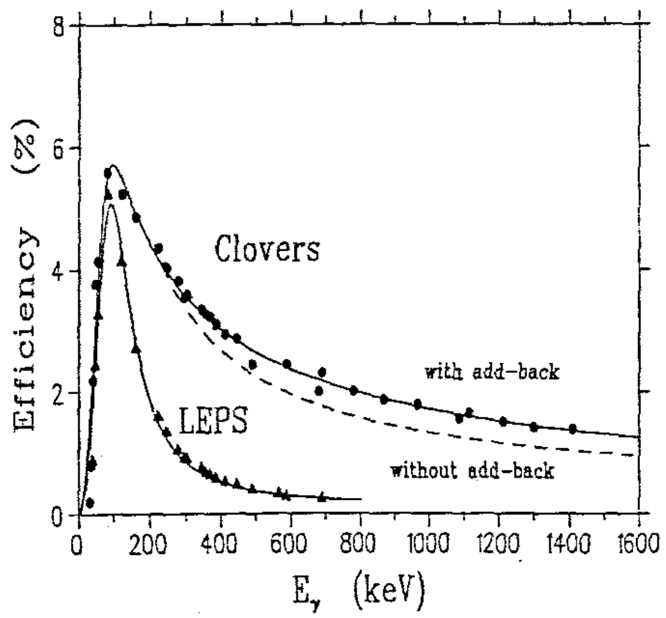

Figure 2-8: The relative efficiency (ε) for the 8 LEPS and 7 Clover detectors measured with ^{152}Eu (filled-circles) and ^{133}Ba (open-circles) radioactive sources mounted on target position by [New98].

CHAPTER 3 RECOIL DETECTOR

This chapter describes the design considerations that have been taken into account for the development of the recoil detector, and the description of the recoil detector in detail.

3.1 Principle of Operation

There are many recoil detectors presently in use around the world; for example,[Bec94][Lei95][Lei97], our recoil detector is based on the design of Ward et al [War83], which was based on the design of Zebelman et al [Zel77]. Its schematic is shown in figure 3.1. This design was chosen because it can detect low energy recoils, distinguish among ions and it could be made to fit in the AFRODITE array. The Ward [War83] recoil detector uses the principle that when a beam hits the target, recoils and fission fragments are produced. Some of the ions produced, and scattered beam, recoil out of the target and are allowed to pass through a thin carbon foil. To distinguish among ions, their time of flight is measured (the time of an ion to move from the target to the carbon foil). When the ions pass out of the carbon foil, electrons are liberated, and they are accelerated by applying a negative voltage on the carbon foil and by grounding the grid behind it. The accelerated electrons are then directed by a magnetic field on to a Micro Channel Plate (MCP), where they are multiplied and detected. The MCP is used because of its fast time response, since the time of flight of the ions are in the range of tens of ns and the MCP has better than 1ns time resolution. The number of electrons liberated from the foil are proportional to the energy lost by the ions passing through, [Cle73] i.e. dE/dX. This dE/dX is proportional to Z^2, where Z is the atomic number of the ion. Therefore, fewer numbers of electrons are liberated for an α particle from the beam as compared to the recoils, so in principle the pulse height from the MCP can distinguish recoils from scattered beam, but for the recoils and the fission fragments, almost the same number of electrons are liberated which makes the difference in time of flight important.

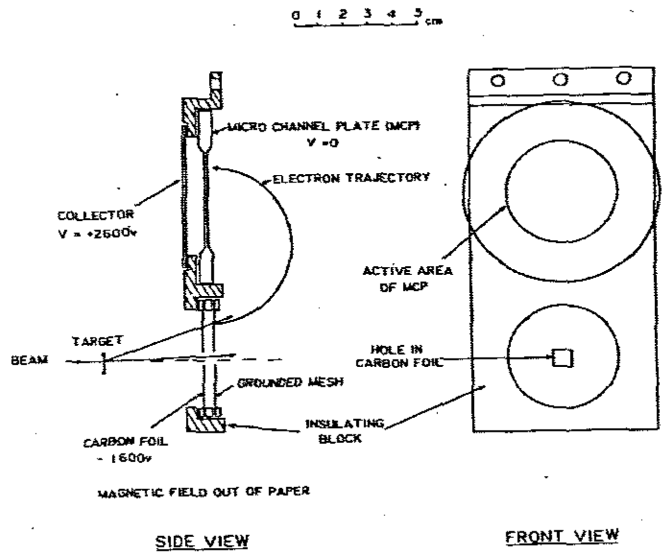

Figure 3-1: Schematic of the recoil detector of Ward et al [War83]

3.2 Design Considerations

Using the ^{232}Th (α, 4n) ^{232}U reaction as a model reaction, the recoiling ^{232}U nuclei would have a velocity of about v/c~0.3% and an energy of about 1 MeV, while the beam has a velocity of v/c~ 19% and fission fragments have velocity of about v/c~4.3% for an energy of 100 MeV. The time of flight calculated for the various ion species assuming a distance of 65 mm from the target to the foil, in the above mentioned model reaction, is as follows: 1ns for the alpha's, 5ns for fission fragments and 68 ns for recoils.

Since the recoils produced from a light beam on a heavy target have low energy, there must be a limit even in the thickness of the target used, so as to allow the recoils to escape from the target. The limit in target thickness has been found using the Monte Carlo Code called SRIM. It was found that no recoils would be able to escape through a target greater than 200μgcm^{-2} thick. These recoils are produced anywhere along the beam's path within the target and due to multiple scattering in the target, they are deflected away from the beam's direction. Due to the fact that SRIM only calculates the scattering of the incident particle from the entrance to the target, the SRIM calculation was done for range of thickness from the smaller up to the larger and the average of all the as thickness was taken. For a 150μgcm^{-2} target, almost 600keV is lost on average by the recoiling nuclei. The number ions scattered as function of angle was also calculated. The results are presented in figure 3.2, which plots the percentage of ions scattered inside a cone subtending a given scattering angle, for a target of 160μgcm^{-2}.

Ideally, to maximize the solid angle, the carbon foil should be placed as close as possible to the target. However, this distance is limited by the necessity of having room for the LEPS detectors to be placed in close geometry. Therefore, the carbon foil was placed 65 mm behind the target. The area of the carbon foil is limited by the size of the MCP, because the dipole magnet preserves the object size (carbon foil) on the image (MCP). The largest available MCP has a dimension of 75x93 mm^2, thus the foil need not be larger than this. With these dimensions, the maximum scattering angle is about 30°, and the SRIM calculations show that about 65% of the transmitted ions should strike the foil.

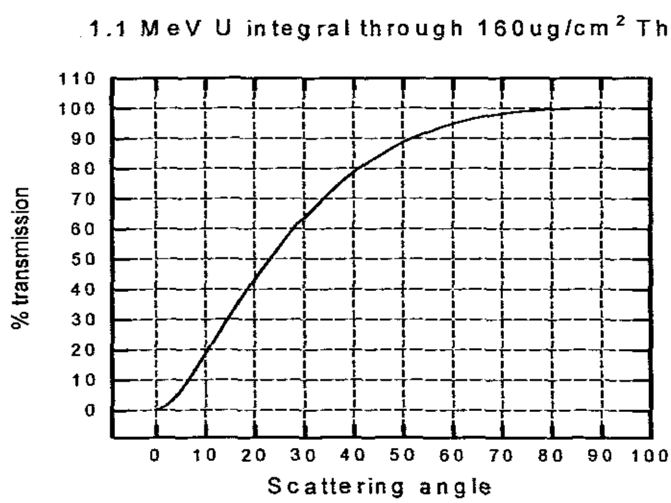

Figure 3-2: The percentage of scattered ions as function of angle.

Since the MCP is rate limited to around 10^7 pps, it is necessary to put a hole in the carbon foil to allow the beam to pass through. The hole results in the loss of geometrical efficiency for detecting the recoils, so its size must be carefully estimated. The hole size in the carbon foil has to be calculated for different reactions, since the scattering of ions depends on the energy of the projectile and its mass.

For example, here it is calculated for the following reaction: ^{181}W (^{20}Ne, xn) ^{196}Po. In this reaction, the beam has 110MeV of energy and the target is about 500μgcm^{-2}. The use of this reaction was also motivated by the desire of checking the heaviest beam that could be used with the recoil detector, since it is known that the heavier the beam, the larger the number of electrons liberated compared to a lighter beam, eventually rate limiting the detector. In order to calculate the size of the hole, the SRIM program was used to calculate the effects of multiple scattering in the target, for the beam, ^{20}Ne and for the recoiling nucleus ^{196}Po. The percentage number of ions transmitted was plotted against the scattering angle from 0° to 90° for both ions i.e. ^{20}Ne and ^{196}Po as they are shown in figure 3.3 and figure 3.4. The size of the hole for ^{20}Ne through ^{181}W was calculated by first assuming that a typical beam current is 1pnA, which is equivalent to 6.25×10^{9} pps (particles per second) or about 10^{10}pps. Since the MCP is rate limited to about 10^{7}pps, the hole must reduce the number of particles per second from 10^{10}pps to 10^{6}pps (assuming 10 electrons are liberated and detected per ion). This has been found to be at 10°, since only 10^{-5} of the ions are beyond this angle as can be seen in figure 3.3. Opening a 10° hole in the foil loses 60% of the scattered recoils, see figure 3.4, but since the carbon foil subtends an angle of 30°, within which 85% of the recoils are scattered, the geometric efficiency of the detector retains a useful 25% efficiency (85%-60%). From this calculation, it has been concluded that beams of mass much greater than 20 are not suitable for the recoil detector, since this efficiency would decline further. Figure 3.2 and figure 3.4 further show that the scattering of the ions depends on the projectile energy and its mass. For example, one may see that at 20° of scattering angle, more ^{196}Po particles are scattered as compared to ^{232}U. This may be due to fact that the heavier beam pushes more particles in its direction of motion due to the higher centre of mass and energy of the system than for the lighter one.

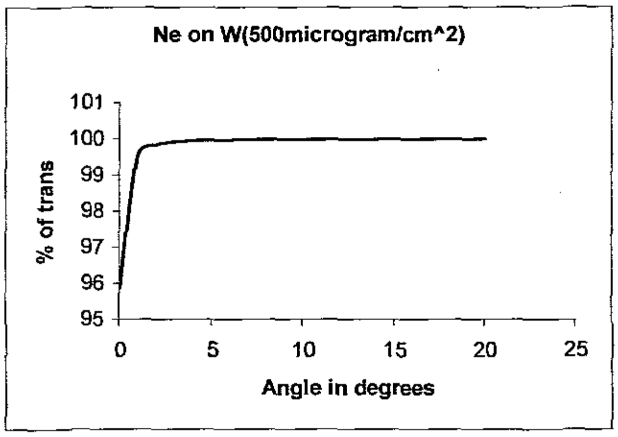

Figure 3-3: The % transmitted ions, when ^{20}Ne go through the target ^{181}W vs. angle in degrees.

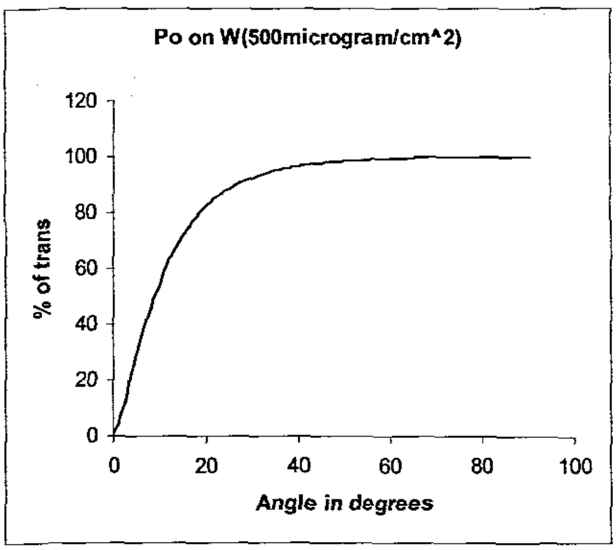

Figure 3-4: The percentage of transmitted ions, when ^{196}Po go through the target ^{181}W vs. angle in degrees.

The thickness of the carbon foil has been chosen so that it would allow the recoils to pass through. For example, in the model reaction, a 10μgcm^{-2} carbon foil is preferred since recoils have low energy, as mentioned above. The liberated electrons are emitted with a typical energy of 50 eV and a cosine angular spread [Bru54][Sch80] [Has92]. The electrons are well focussed by accelerating the electrons to about 1.6 keV, which is close to the maximum MCP efficiency. The size of required magnetic fields to deflect the electrons onto the MCP should be known.

The magnitude of the magnetic field was first calculated by assuming that the energy of the electrons liberated when ions go through the carbon foil is 50eV and that they are accelerated to 2keV. Using equation 3.1, the magnitude of magnetic field was calculated, since the radius of curvature of the electrons was determined by the size of the MCP and the need for a compact geometry. This was done in order to get an idea of the magnetic field strength, which helped in getting the acceleration voltage in table 3.1. The radius of curvature was just the distance from the center of the carbon foil to the center of the MCP. The design parameters of the recoil detector are tabulated in table 3.1 and the equations used to calculate some of the recoil detector parameters are shown next to table 3.1. Some of these equations were taken from [Zel77] and are proved in Appendix. A permanent magnet was chosen over an electromagnet for simplicity but even permanent magnets are divided into different types depending on the type of materials they are made of. For our recoil detector a betaflex magnet was chosen because it was easy to cut with any tool to the length that would fit on the side of the recoil detector chamber. Betaflex magnet is made of flexible rubber-like plastic with barium or strontium ferrite powder imbedded. In order to make the fields lines between the poles uniform, extra magnetic material or a belt of magnets can be added to the edges of the magnet. The magnets that are added on the edges are called shims. The dimensions and position of the shims must be known so as to make the magnetic fields uniform. Therefore, more detailed calculations using the program Vector Fields were performed by Garret de Villiers at iThemba LABS. The path of the electrons in the magnetic field with is shown in figure 3.5. Garret found that the shims of 15x5 mm^2 thickness were necessary to make the fields uniform as it can be seen in figure 3.5 where the image is almost of the same size as the object.

$$B\rho = \frac{\sqrt{E_k^{\,2} + 2E_k E_0}}{Qc} \ldots \qquad 3.1$$

$$\rho = 3.38\sqrt{V}/H \text{ (bending radius)} \qquad 3.2$$

$$t = 179/H \text{ (time of flight for} 180^0 \text{ deflection)} \qquad 3.3$$

$$t = \frac{33.7d}{\sqrt{V}} \text{ (time of flight when starting from rest in a uniform electric fields)} \qquad 3.4$$

$$\theta = \frac{1\omega t}{2} \text{ (with } \omega = 1.7 \times 10^{-2} B) \quad 3.5$$

Parameters	**Value**	**Unit**
Magnet		
Radius of curvature ρ	6.25	cm
Field B	22	G
Pole gap	14	cm
Acceleration voltage V (eq. (2)	1655	V
Approx. time of flight t (eq. (3))	8.1	ns
Acceleration region		
Carbon foil diameter	8	cm
Foil harp separation	1	cm
Time of flight (4)	0.81	ns
Exit angle (5)	0.31	rad
Anode (MCP)		
Maximum Applied voltage	2000	V

Table 3.1: The parameters of a recoil detector.

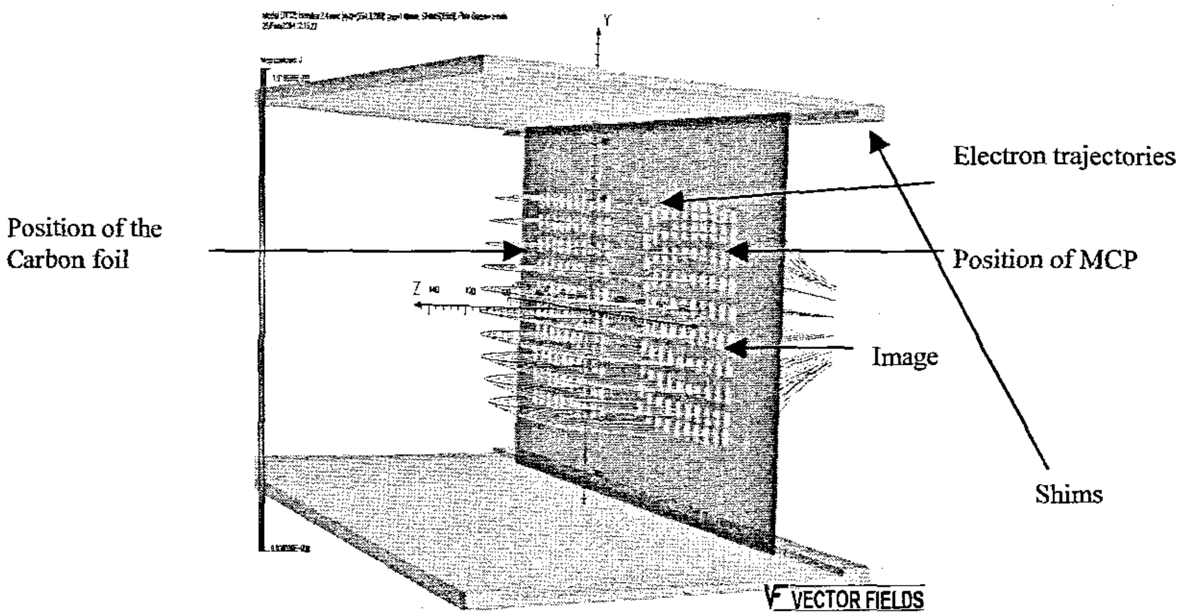

Figure 3-5: The projection of electrons in the magnetic fields, the electrons path starts in z-direction and the magnetic field in y-direction. Note that the object is almost preserved by the image.

3.3 The Micro Channel Plate

Since the time of flight in our model reaction is in the ns range, the electron detector that should be employed for our recoil detector should be a very fast device. Therefore, a MCP was chosen and is discussed in detail here.

3.3.1 Construction and Operation principle of MCP

The micro channel plate is a very fast device that converts charged particles and photons into a signal. The construction and operating principle is shown in figure 3.6.

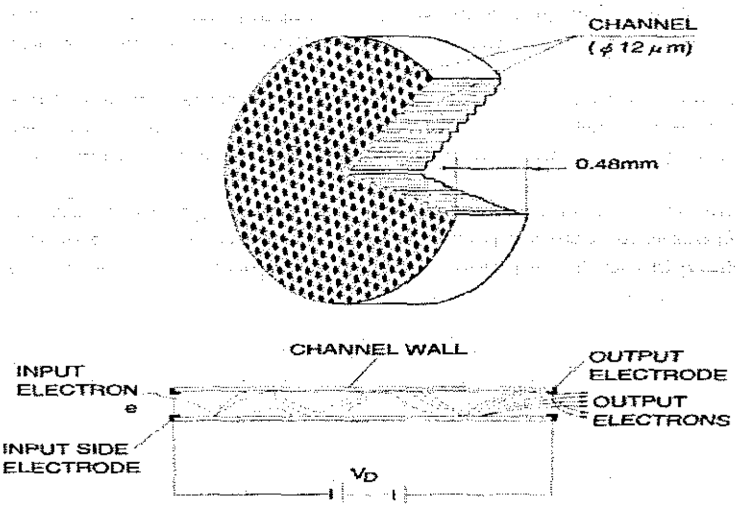

Figure 3-6: Schematic Construction and operating principle of MCP [Tec94].

The MCP is formed by a number of small tubes with same length and diameter. These tubes are called channels. When the electrons or any charged particles enter a tube, they are accelerated by means of electric fields formed by voltage V_D that is connected across both end of the tube as shown in the bottom part of figure 3.6. As they are accelerated, they move in the circular path to strike the opposite wall. When electrons hit the tube's wall, their number is multiplied i.e. a large number of secondary electrons is produced. This process occurs up to the end of the tube for different tubes simultaneously. At the end of the channel large number of secondary electrons is released to be converted into a signal by the signal processing electronics.

3.3.2 The Gain Characteristics of MCPs

The single stage MCP cannot exceed a gain of 10^4 due to noise that appears after this gain has been exceeded [Tec94]. The noise is caused by ion feedback i.e. the response from the ionized gases remaining in the channels. More gain can be achieved if two MCP's are used in a chevron arrangement shown in figure 3.7. The chevron arrangement has the advantage of increasing the gain and reducing the noise due to positive ion feedback [Lam01]. The gain characteristics of MCPs with different number of stages are shown in figure 3.8.

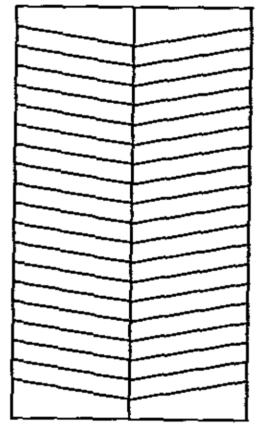

Figure 3-7: The chevron arrangement of a two stage MCP.

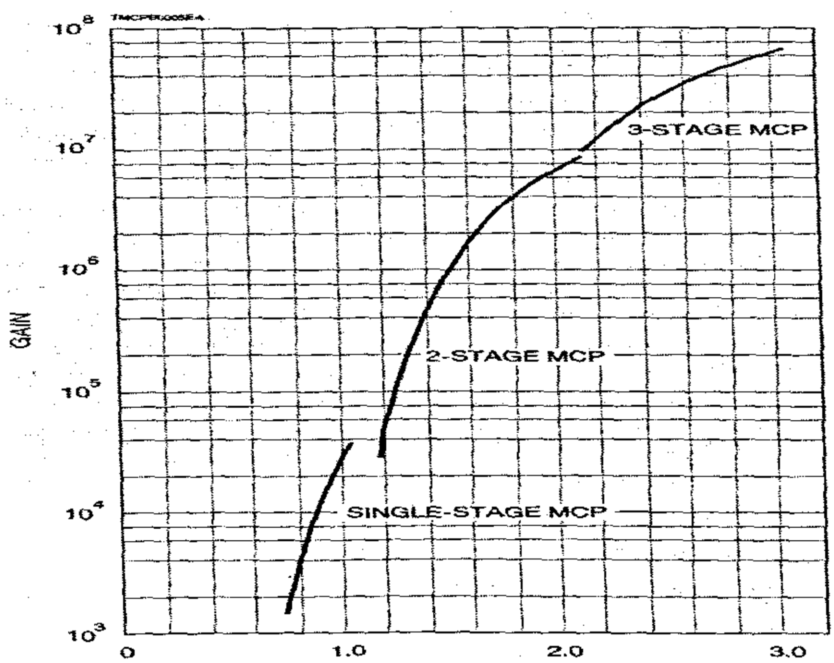

Figure 3-8: The gain characteristics of MCP with different stages [Tec94].

In figure 3.8, it is clear that the maximum applied voltage for single stage MCP is 1kV, for 2-stage is 2kV, and for 3-stage is 3kV.Therefore, each stage needs 1keV. It can also be seen that the higher the number of stages the higher the gain.

The gain required of the MCP detector in the present application was chosen by assuming that a reasonable signal size is 50 mV, a 50 Ω resistance, a 5 ns wide pulse, and 50 electrons emitted when a U atom passes through the10μgcm^{-2} carbon foil. Ohms law ($V=IR$) and the current law ($I=\Delta Q/\Delta t$) were used to calculate the gain required for our recoil detector. Using Ohms law, the instantaneous current was calculated:

$I=\frac{V}{R}=\frac{50mV}{50\Omega}=1mA$. Then the total charge in the pulse is

$\Delta Q=I\Delta t$=1mAx5x10^{-9}s =5x10^{-12}C=30x10^{6} electrons. That implies, 50 electrons need to be amplified to 30x10^{6} electrons, implying a gain of ~10^{6} is required. A gain of this magnitude implies a two stage MCP as seen in figure 3.8

3.3.3 Vacuum Requirements

The MCP can only work at a vacuum less than 10^{-6}mbar due to dark current that increases at higher pressure. The dark current is considered to be from many factors: thermionic emission and electric field emission from channels walls, the ionisation of residual gases, local discharge by a high electric field and the photoelectron emission produced in electric scintillation of the MCP supports [Tech94][Lam01]. Therefore, the high voltage can only be applied in the MCP if this requirement is reached, otherwise the MCP will be damaged. Therefore, to protect a recoil detector MCP, it has to be kept into a vacuum. The manufacturer has measured the dark counts of our recoil detector 2-stage MCP and found it to be 2.0 Counts/sec/cm^2. This was done at an acceleration voltage of –300V and the voltage on the MCP was 2200V, at this voltage the gain was 2.1x10^{7}.

3.3.4 The specifications of a Recoil detector MCP

MCP's are available in different shapes with different physical and electrical specifications. The figure showing the shape of the recoil detector's MCP and some dimensions are shown in figure 3.9 with its tabs on the side, while its physical and electrical specifications are tabulated in table 3.2.

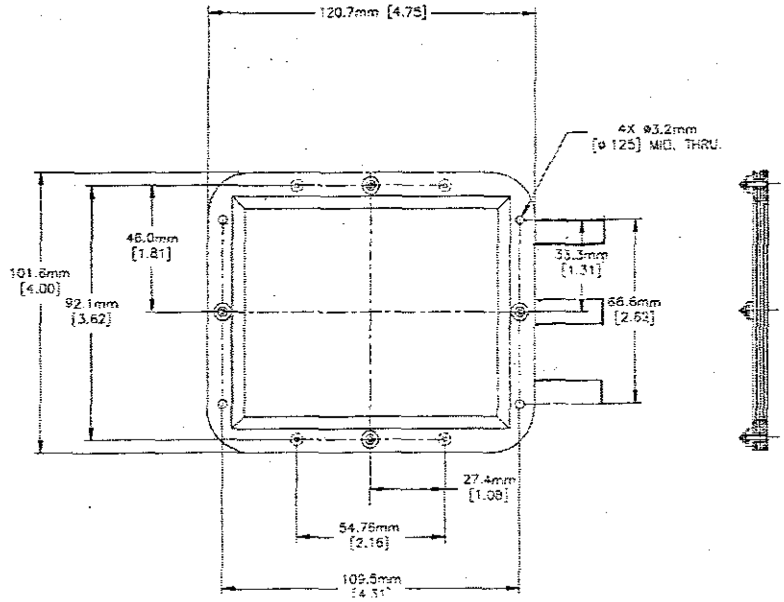

Figure 3-9: The schematic showing the shape and dimensions of a recoil detector's MCP. Tabs making electrical connections with the front, back of the MCP and the anode are shown on the right.

Physical characteristics of MCPs	Specifications
Quality Area Dimensions	75 mm x 93 mm
Center to Center Spacing	32 μm Nominal
Pore Size	25 μm Nominal
Bias Angle	8° ± 1°
Open Area Ratio	45% Minimum
Quality level	Detection
Electrical Characteristics of Detector	**Specifications**
Electron Gain @ 2000 Volts	4 x10^6
Bias Current Range @ 2000Volts	75-300 μA
Resistance	7-27 MΩ Reference
Pulse Height Distribution @ 2000 Volts	175% Maximum
Linear Output Current Density (μAcm^{-2})	Typical 10% of Bias Current Density

Table 3.2: The electrical and physical specifications of a recoil detector MCP.

3.4 Mechanical Construction

Since the MCP requires a very low pressure (10^{-6}mbar) for HV to be applied to it, the recoil detector mechanical construction should consider this requirement. Since the electrons emitted from the carbon foil have to be accelerated and bent into the MCP, the space for magnets and the carbon foil have to be considered, otherwise the electrons would not be accelerated and detected. The negative voltage must be applied to the foil and there must be a space that separates the carbon foil from ground to accelerate electrons. Since the recoil detector is using HV, the interference among cables must be some how avoided. In order for the accelerated and bent electrons to hit the MCP, they must be some how focused to the MCP. The fact that MCP requires a very high vacuum means that the carbon foil should also be in vacuum too, therefore, the pumping process should consider the sensitivity of carbon foil. Since the time of flight is very important the distance between the target and the carbon foil should be kept short as discussed i.e. 65 mm. Optimization of beam focusing on the target requires a viewer and a camera. This mechanical construction consideration has to take into account that the recoil detector should fit into the AFRODITE array.

A photograph of the recoil detector undergoing vacuum testing is shown in figure 3.11 while a schematic picture is shown in figure 3.11. The target chamber at the center of figure 3.10 and 3.11 has 1 mm aluminium windows to allow low energy (<100 keV) gamma rays to be detected by LEPS that surround the target chamber. The big box in figure 3.11, which is attached to a target the chamber, is the recoil chamber that houses the internal parts (MCP, grids, carbon foil) of the recoil detector. The internal parts are mounted on an insulating block, which is attached to the base of the recoil detector chamber as seen in figure 3.12, where some of the internal parts are also shown. The insulating block isolates the HV from the aluminium chamber. In the bottom half of the insulating block is a recess for the carbon foil, upon which a plate for connecting negative voltage to the foil would be placed. A spacer (4) separates the grid from the foil. The top half is where the MCP sits as seen figure 3.13, where the MCP is shown mounted with its tabs facing up. A plate (6) prevents electrons following non-circular orbits reaching the MCP. The insulating block is mounted on the detachable base (1) of the recoil chamber, by which access is gained to the inside of the chamber. The base contained the electrical feed through (3), (5).

The wiring circuit for connecting high voltage to MCP is shown in figure 3.14. Capton wire was used for all the internal connections of the recoil detector because of its HV tolerance and good vacuum properties. Resistors 1 MΩ and 0.1 MΩ in figure 3.14 act as a voltage divider which allow different voltages to be applied in the anode and the MCP tube so as to accelerate the electrons inside the MCP while a capacitor of 1 nF reduced the noise in the MCP by shorting it to ground and a 2.2 nF capacitor allows the AC signal to reach the amplifier, while isolating it from the HV. The slots on the sides of the insulating block as seen in figure 3.13 are there for the cables from the MCP, foil and grids to go to the feed through at the bottom at the base of the Al box without touching each other thus avoiding interference.

To the right hand side of the chamber target chamber in figure 2.11, is a cone-like pipe to accommodate an external camera and controls for a ruby viewer used for focusing the beam. The viewer moves upside down like a hand and it is controlled automatically by a long rod connected to a pneumatically controlled piston. Due to the sensitivity of the carbon foil, the arm like pipe in both figure 3.10 and figure 3.11 has been made so as to pump on both sides of carbon foil simultaneously in order to balance the force that may otherwise damage the carbon foil during the process of pumping down.

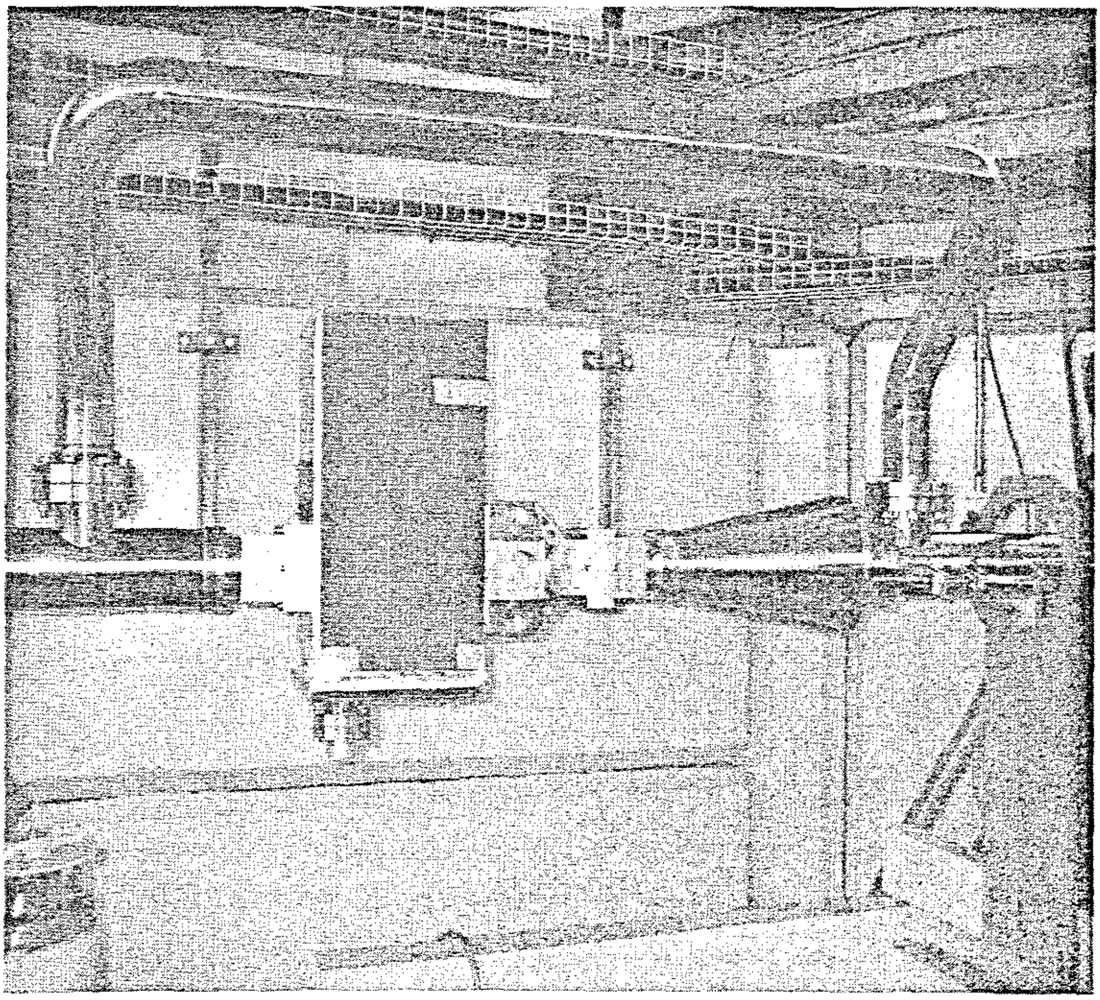

Figure 3-10: The recoil detector undergoing vacuum testing.

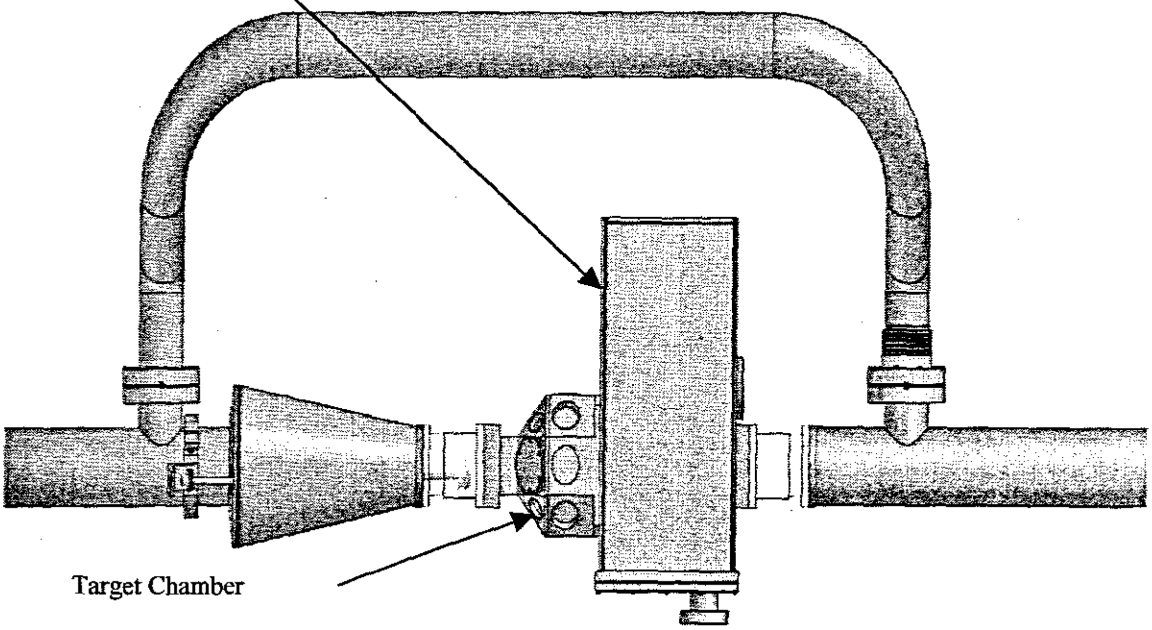

Figure 3-11: The schematic of the recoil detector

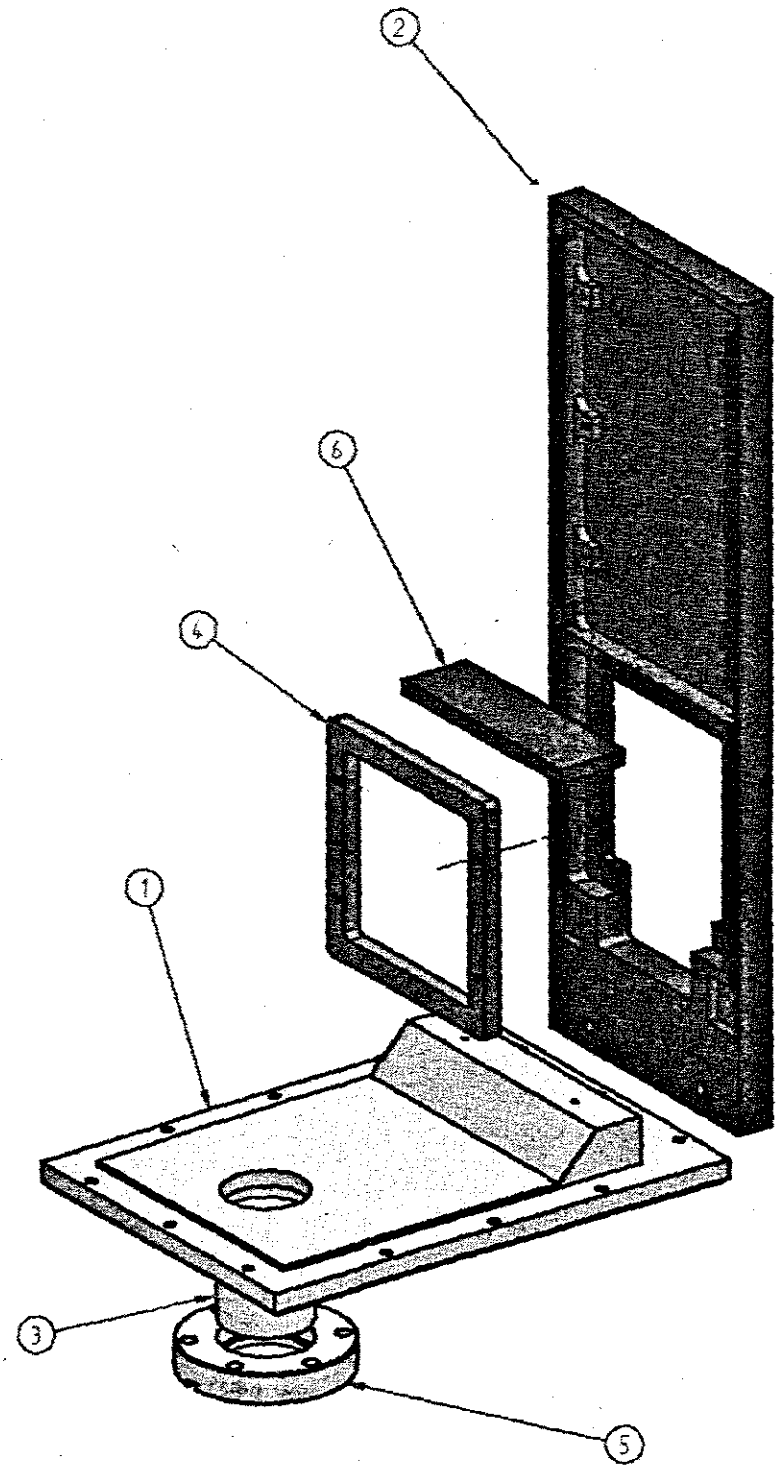

Figure 3-12: The insulating block (2) and its base (1) with feed thru (3 and 5), spacer (4) and the collimator (6).

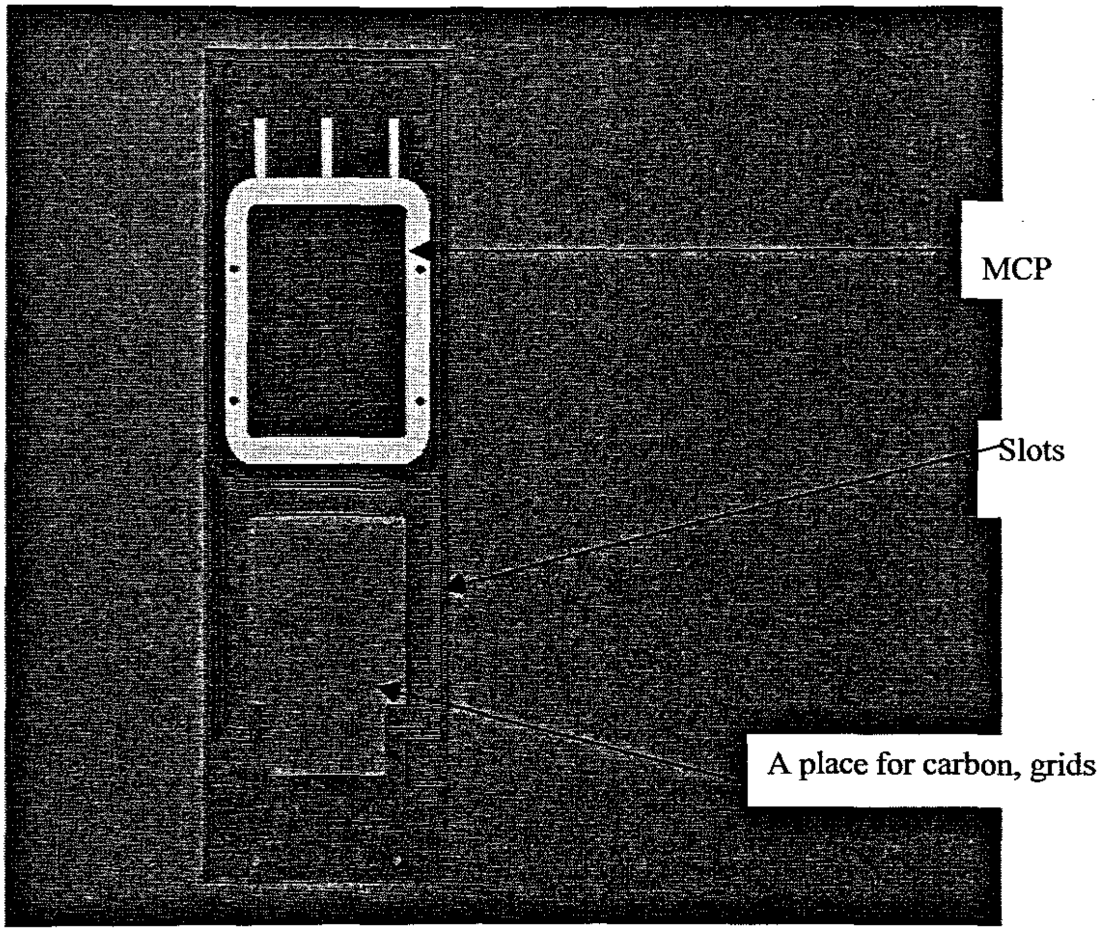

Figure 3-13: The block diagram that holds the internal parts a recoil detector.

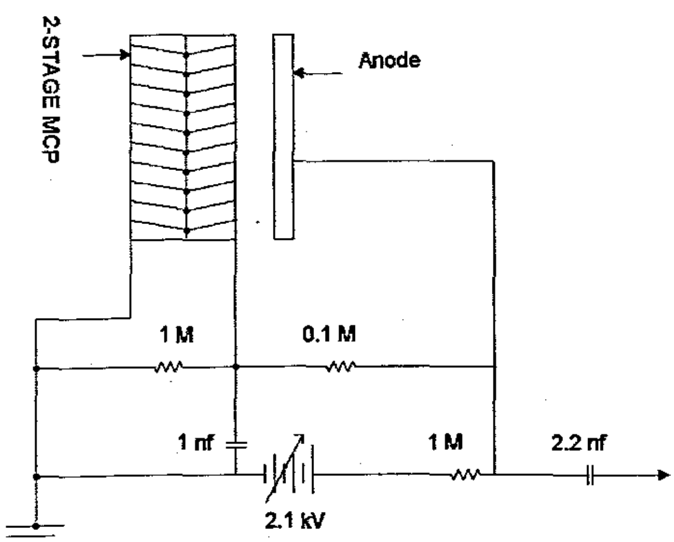

Figure 3-14: The wiring circuit of the 2-stage of the recoil detector MCP.

3.4.1 The Process of Mounting a Carbon Foil.

Because the carbon foils are very thin, special care is required to mount the foils on their frames. The carbon foils came from the manufacturer (Arizona Carbon Foil) coated on a 10x11 cm^2 glass and were floated and mounted on 10x10 cm^2 aluminium frame shown in with an active area of 8x8 cm^2, using the process described in the following steps.

Equipment used in the mounting process: 25 litre water container, 15 litre tank with a tap, distilled water, alcohol, one meter pipe (3cm diameter) and an aluminum stand to hold the glass plate at 45°, and an aluminum holder to hold the frame vertically.

I. A 25 litre container was filled with a solution of 17% alcohol and distilled water. The reason for the alcohol was to reduce the surface tension of the water, which could damage the foil.

II. The carbon-coated glass was taken out of its container and scratched on its edges, so that it would float easier with the alcohol solution.

III. The scratched carbon foil was put on the 45°-aluminium stand, figure 3.15 shows the picture of carbon-coated glass on the 45°-aluminum stand.

IV. The 45°-aluminum stand, as seen in figure 3.15, and aluminum frame holder were put at some distance parallel to each other in an empty 15 litre tank as can be seen in figure 3.16.

V. The 10x10cm^2 frame was cleaned with alcohol and put in its slot in the frame holder as can be seen in figure 3.16.

VI. Using the pipe, the distilled water and alcohol solution was drained slowly from the 25 litre water container into the 15 litre tank; this was done at a very slowly to avoid the damage of the foil by vibrations. The tank was filled until the carbon foil completely floated off the glass and floating on the surface of the water above the aluminum frame. Figure 3.16 shows the picture of a carbon foil floating above the frame.

VII. After the water level was above the top of the frame, with the carbon foil floating on it, the foil was moved by blowing on it gently and slowly until its edge was above the frame.

VIII. While the edge of the foil was above the frame, the water was taken out very slowly using the tap (for example it took 1.5 hours to empty the tank) in the tank until the foil was mounted all over the frame. Figure 3.17 shows a carbon foil as water being moved out slowly off the tank.

IX. The mounted foil was left in the empty fish tank for an hour for it to dry and then taken to safe place.

Figure 3.18 shows the picture of a mounted carbon foil inside the tank. The frames were modified to have a support system in their middle because the foil would break at a point 2 to 3 cm from the edge.

Precautions: Air conditioning must be off during this process until the foil is taken to a safe place, no movement of anything is allowed during this process, since it may cause vibrations on the water and thus damage the foil. Patience is very important to a person mounting the foils. This process has only been successful in mounting the thicker foils i.e. from $20\mu gcm^{-2}$ upward.

Figure 3-15: Carbon coated glass on a 45° aluminum stand.

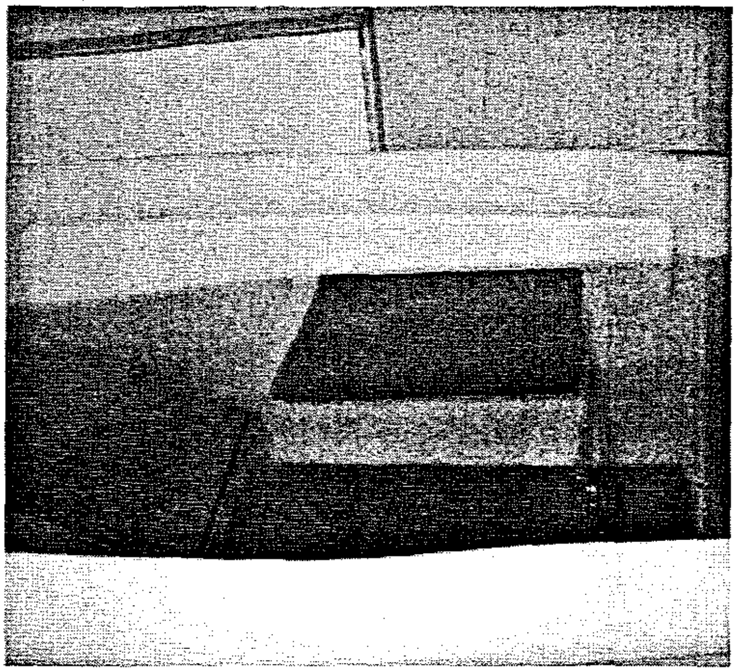

Figure 3-16: The carbon foil floating in the tank after the water level has risen above the frame the foil has floated free of the substrate. The foil is the moved gently until one edge lies above the frame. The water is then moved slowly out of the tank.

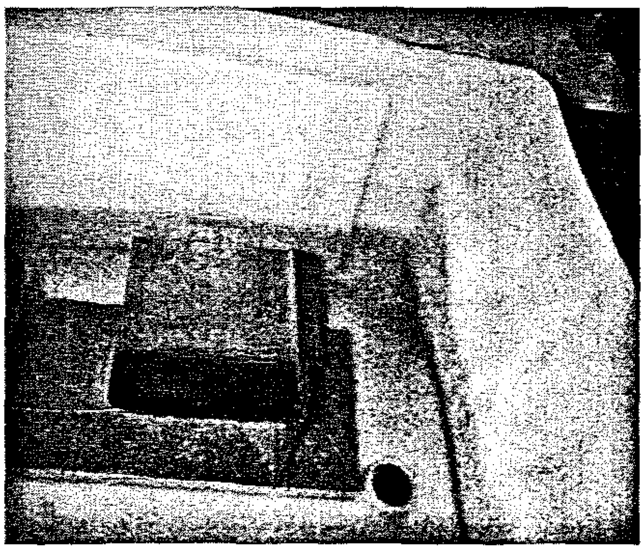

Figure 3-17: The carbon foil resting on frame as water moved out slowly out of the tank.

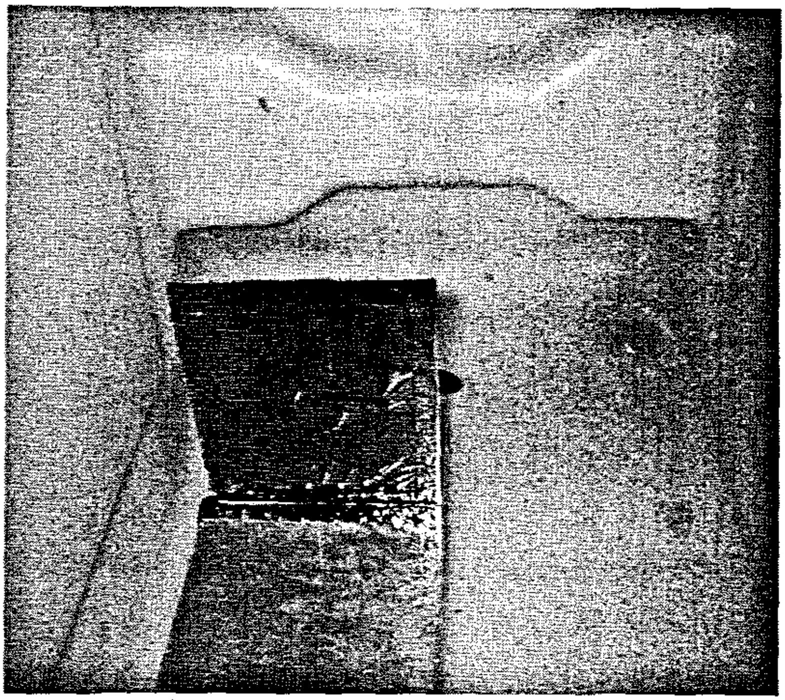

Figure 3-18: The carbon foil mounted on a frame.

3.4.2 The process of making a hole in a carbon foil

An accident that happened in 1971 during a public-relations event at Los Alamos discovered that a foil in air can be oxidized (to gas) in a localized area simply by flashing a photographic flash bulb near it. In this event people were busy taking some photos and there were carbon foils around them and they eventually discovered that their flashes corroded the foils. From this accident carbon foils have been known to be affected by exposure to intense flashes of light. Therefore, the process of making a hole is based on this behavior of carbon foils. The president of ACF-Metals, Dr. John O.Stoner, Jr, reported this accident to us via fax.

The hole calculated as discussed in section 3.2 was made using flashes of light from camera flash through an aluminium mask with a hole in it of the same size as the calculated hole. The mounted foil and the aluminum mask were put in an aluminum stand with a slot to mount the carbon foil and one for the aluminum mask. The separation between two slots was 1cm. Using the camera flash, the light was flashed directed at the aluminum mask until a hole was made in the carbon foil.

3.5 A Recoil Detector Test with a ^{252}Cf fission source

For the test of the recoil detector a spontaneous ^{252}Cf fission source was placed in a position facing the carbon foil so that fission fragments from the source would hit the carbon foil. The block circuit diagram of the test is shown in figure 3.19. The chamber was pumped down to 10^{-1} mbar, via a small pumping valve (to avoid damaging the foil) down, and then via a bigger valve. After five days all the gases inside the microchannels were pumped out, corresponding to a pressure of the 1.2×10^{-6} mbar, whereupon the high voltage was applied very slowly as described in the MCP manual, up to 1.8 kV, which is equivalent to a gain that is more than 10^6 as shown in figure 3.5. After that, a negative acceleration voltage was applied to the foil via the feed through, with the grid grounded, with the output from the MCP being monitored on the oscilloscope. At about 1640V, which was almost equal to a calculated acceleration voltage, the signal in figure 3.20 was observed. The signal observed was believed to be the real signal from the MCP (with ringing due to mismatching of impedance). This was proved by reducing the voltage of the foil, which reduced the signal until it disappeared and reappeared when the voltage on the foil was increased above the threshold corresponding to the required for the correct trajectory of the MCP.

To reduce the ringing the length of the anode cable outside the chamber was reduced to 15cm. The ringing, however, persisted. To better match the impedance, a test was done with a potentiometer between signal and ground of the oscilloscope (1MΩ input impedance on the scope) with the potentiometer resistance close to 50Ω the signal observed to have only one ring is shown in figure 3.21. To get rid of this last ring, the MCP was turned around so that tabs faced the feed through, to further shorten the cable length, (but this required an increase of the negative acceleration voltage to 2900V due to the increase in the radius of curvature) and the capton wire was replaced with 50Ω copper-shielded cables. During this attempt of getting rid of the last ring, a signal suddenly appeared at 500V on the foil, instead of about 2900V. This was surprising until it was proved through extensive testing of the chamber that the feed through was breaking down. The feed through was taken out and replaced by the three new feed throughs. These new feed throughs were also found to be breaking down at about 1500V. New feed throughs were ordered but delivery took three months, leaving no time for this part of the project to be fully completed.

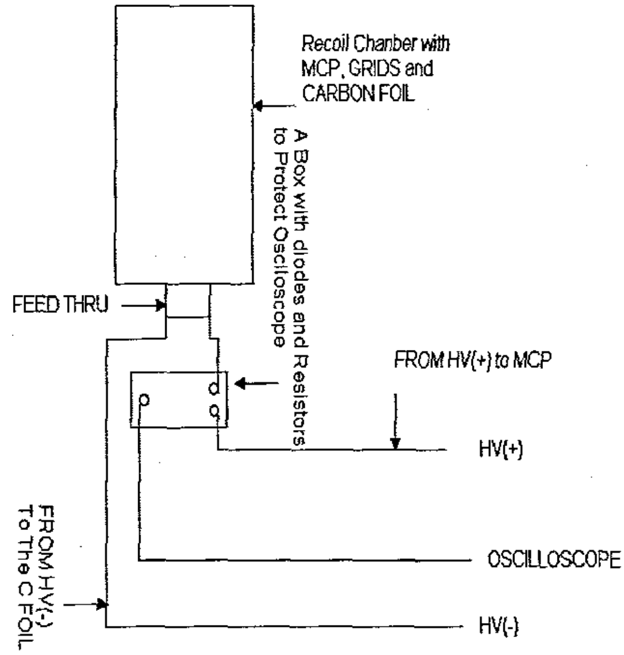

Figure 3-19: The-block circuit of a recoil test with 252Cf fission source

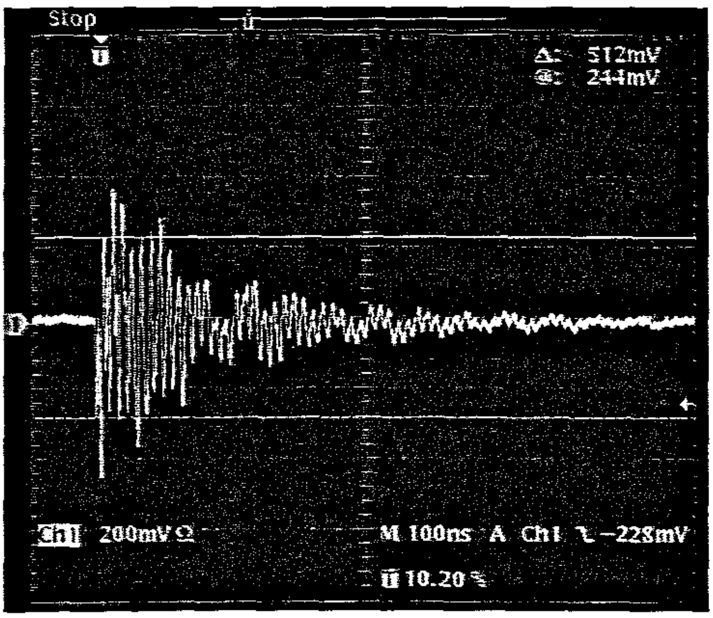

Figure 3-20: The signal observed for the first test of MCP with ^{252}Cf fission source.

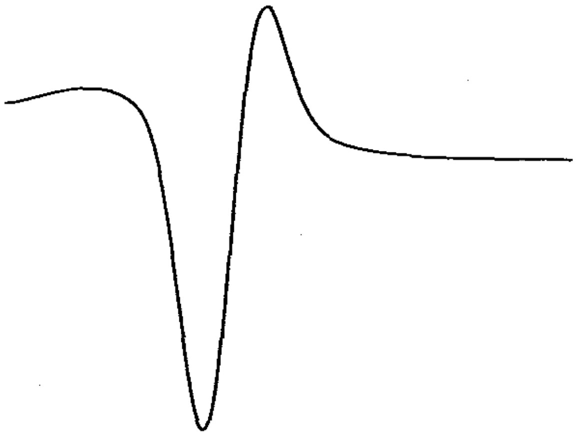

Figure 3-21: The signal with one ring seen during the recoil detector test, when the test was done with pot between signal and ground, with nearly 50Ω resistance (Oscilloscope input impedance at 1 MΩ).

CHAPTER 4 SOLAR CELL ARRAY

This chapter describes the design considerations that have been taken into account before the development of the solar cell array detector and the solar cell array in detail.

4.1 Design Considerations

The solar cell array is developed as an attempt to use it as a fission veto (i.e. to be used in detecting fission fragments which are in coincidence with γ-rays detected by AFRODITE, thus allowing them to be neglected) in the model reaction. Since the fission fragments are emitted in any direction during the fission process, a solar cell array suitable for detecting them ideally has to cover a solid angle of 4π, although this actually cannot be achieved because space is needed for the target holder, the beam entrance and beam exit.

The use of solar cells was motivated by their response to different incident ions due to the funnel effect [Lia88] [Bra00] [Cl82], to their cheap price and to their flexibility for constructing a array that can fit into AFRODITE. The funnel effect (discussed in section 4.1.1) is higher for heavy ions compared to light ones. Therefore, in a high fission channel reaction, for example, in the model reaction (α + ^{232}Th), the solar cells would be insensitive to scattered beam due to the low funnelling efficiency for α particles, but sensitive to the fission fragments.

4.1.1 The funnel effect

When an ion passes through the material it loses energy via coulomb interaction with the electrons, so that some of its energy is lost to the electrons which are thus liberated. The energy lost per-unit-path length is described by the Bethe-Bloch equation. Which relates the energy lost per-unit path length of the particle to the atomic number of the particle as shown in equation 4.1.

$$\frac{dE}{dX} \propto Z^2, \qquad 4.1$$

where Z is the atomic number of the projectile.

In the above equation one may see that the higher the atomic number the more energy would be lost by ion per-unit-path length. That is to say more electrons are liberated if a massive ion passes through material.

Materials in the world are divided into many types, for example conductors, insulators and semiconductors. These types can be distinguished from one another by the property called electrical conductivity i.e. the ability of the material to conduct electricity. Conductors are those materials that are able to conduct electricity due to the presence of charge carriers in their structures [Wah01]. The charge can be electrons, ions, etc. Insulators are those materials that are not able to conduct electricity due to absence of charge carriers in their structures and Semiconductors are those materials with both properties of insulator and conductors.

In solid materials electrons fill different bands with different energies, the last filled band is called valence band and next highest band is called the conduction band. The conduction band is the one that is occupied by electrons that play a role in conduction i.e. charge carriers. Electrons in a completely filled band cannot move but can jump to the higher level, which needs energy, while in a partially filled band they can move since there are still some free states to move to.

In an insulator material the valence band is filled and the gap between it and the conduction band is very big. In a semiconductor valence band is partially filled and the gap between the valence band and conduction band is small. In conductor material valence band is partly filled and the conduction band overlaps the valence band. Because of the small separation between conduction band and valence band in semiconductor materials, they behave like an insulator at T=0, since there is no energy to raise electrons to the conduction band, but at T>0 they behave like conductors, since some of electrons are raised by thermal energy into the conduction band. Due to this behaviour they are used in making solar cells. These semiconductors are known to be in group four of the periodic table. i.e. they are having four electrons in their valence band. Semiconductors can be classified into n-type or p-type and n-p type, etc material. The n-type material is the semiconductor that is doped with an element which has five valence electrons, where four bond with four from the semiconductor while the other one remains unbound in the material, so that it plays a role in conduction. The p-type material is one doped with an element, which has only three valence electrons. These three bond which leaves the remaining one free to move out of the valence band into the conduction band, leaving a hole which acts as the charge carrier.

An n-p type semiconductor is formed when n-type and p-type are mixed together. If n-type and p-type are mixed together, the electrons move from the n-type and holes move from the p-type to the n-type by the process called diffusion i.e. the movement caused by the different concentration. The electrons that move across the boundary they combine with hole and the depletion region is formed and charge carrier are left behind and unable to move. Solar cells are nothing else but a n-p type semiconductors as shown in figure 4.1, which shows what happens if a charged particle or ion enters the depletion region of the solar cell. When an ion immediately penetrates through the depletion region electrons and holes are formed in its path due to the due the energy lost by ion. This creation of electrons-hole below the depletion region causes the depletion region to collapse due to the rearrangement of charge carriers that are now below the depletion region [Bra00][Mcl82]. This arrangement is achieved by the strong electric field in the depletion region, which quickly reproduces a redistribution of carriers until many of impurities are shielded. Impurities are those atoms that are introduced in a pure semiconductor material by doping process so as to form n-type or p-type semiconductors. The redistribution of charge carriers so as to shield impurities results in the shrinking of depletion region. After the depletion region has collapsed and impurities have been shielded the electric field push holes down so that they are below the negative acceptor that they were screening thus expanding the depletion region. This process of expanding the depletion region is termed funnelling. Since the energy loss per unit path is proportional to the atomic number of an ion, considerable funnelling occurs for heavier ions, since more hole-electron pair is created. After the carriers have been collected the depletion region would return to its stable state. Thus a solar cell is insensitive to an alpha beam, since alphas have poor funnelling efficiency, but is sensitive to fission fragments, which have much higher Z.

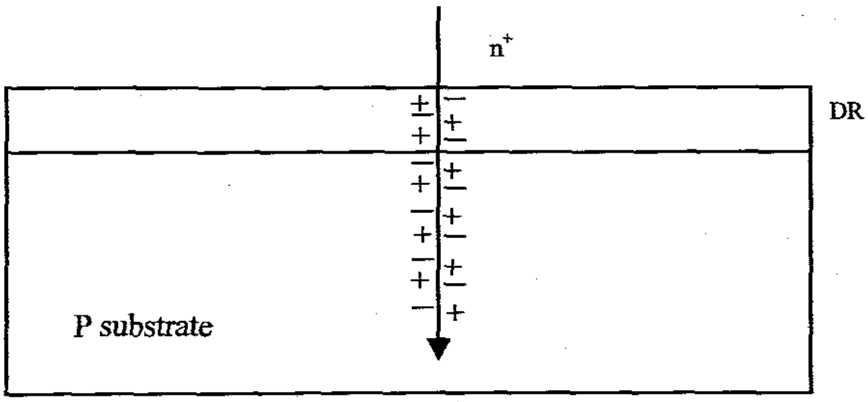

Figure 4-1: The demonstrating of the process that occurs when an ion passed through the depletion region (DR) of the solar cell.

4.2 Construction of the solar Cell Array

The solar cell array developed at iThemba LABS is comprised of fifty-one $1cm^2$ solar cells arranged in a cubic array as shown in figure 4.2, where it is shown placed inside the AFRODITE target chamber on the target ladder, with the ruby to allow the focus of the beam. The cube seen inside the AFRODITE target chamber is made of a plastic and has 9 solar cells placed in each side. This array has a solid angle covering almost 74% of 4π, which was calculated as discussed in section 4.2. Three solar cells were removed for a target holder and for beam entrance and exit. The solar cell array was arranged in a cubic shape because it was simplest shape to make.

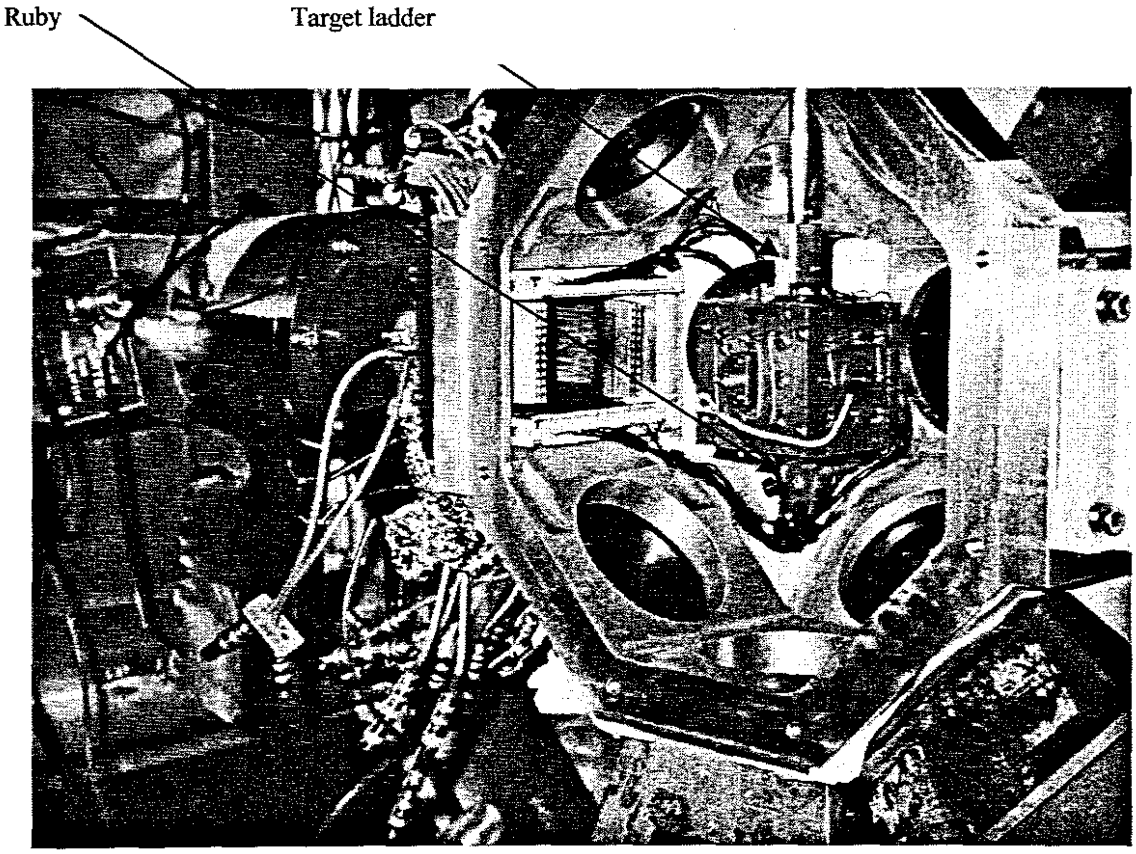

Figure 4-2:*A solar cell array placed inside an AFRODITE target chamber.*

4.3 Calculation of geometrical efficiency

The geometrical efficiency of the solar cell array was calculated by taking the inside area as its active area, the dimensions of which are shown in figure 4.3. The inside area of the cube was taken to be equivalent to a solid angle of 4π, and the efficiency calculation is shown below:

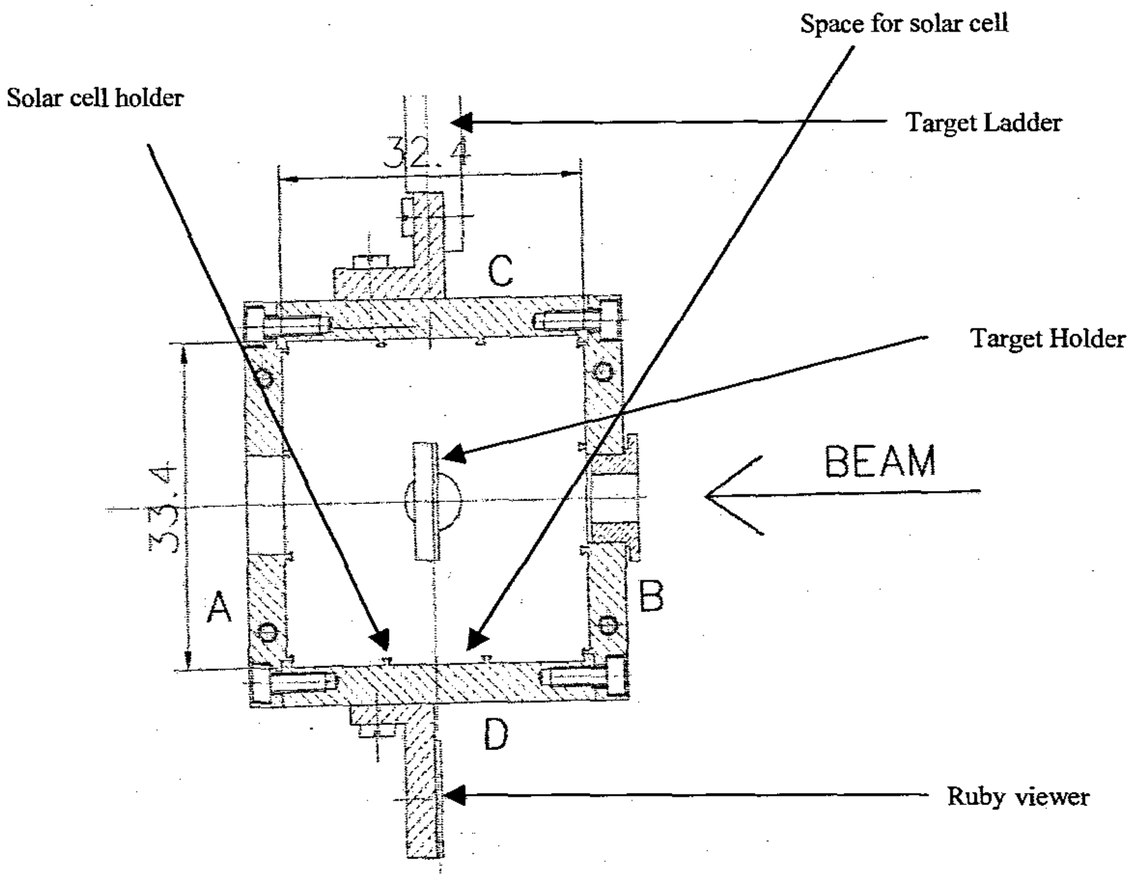

Figure 4-3: The dimensions of side view of the inside area of the solar cell array.

The inner area of the solar array cube was = 6x33.4x32.4

$= \underline{6492.96mm^2}$

Area of each solar cell after soldering it inside the cube=10.1x (10.1-0.8)

$= \underline{93.93mm^2}$

The 0.8 mm that was subtracted was due to an electrical contact on the face of the cells and the area covered by the slots holding the solar cell in place (see figure 4.3). The cube has six sides and each side could mount 9 solar cells.

The active area of 9 solar cells in each cube's side= 6x9x93.93

$= \underline{5072.22mm^2}$

In the solar cell cube, three solar cells were removed for beam entry and exit and also for the target.

Thus, the active area of solar cells after removing three solar cells

$$= 5072.72-(3x93.93)$$

$$\underline{= 4790.43mm^2}$$

The efficiency was calculated as the percentage of 4π

Efficiency of solar cell array (51 solar cells) (geometric one) = $\frac{4790.93}{6492.96}$=74% of 4π.

CHAPTER 5 EXPERIMENTAL METHODS AND EQUIPMENT

The chapter describes the experimental methods and equipments used for a solar cell array test experiment.

5.1 Targets

The target that was available for solar cell array test experiment was 1mgcm^{-2} of ^{232}Th. This thickness was suitable for solar cell test since it was proved by SRIM that the fission fragments could be scattered out of such thickness and thus detected by the solar cell array. The thickness was confirmed by performing the RBS (Rutherford back scattering) at MRG (Material Research Group at iThemba LABS).

5.2 Beam energy

The two *solid-pole injector cyclotrons namely* SPC1 and SPC2, *in conjunction with* the Separate-Sector Cyclotron (SSC) can be used to accelerate ions to the required energies. The SPC1 (K=8MeV) is used to accelerate light-ions while SPC2 (K=10MeV) is used to accelerate heavy-ion and hydrogen ion beams. The SSC has K=200MeV. The K value represents the maximum energy that protons in the cyclotron can reach, for other ions the following formula is used to determine the maximum energy (T) that the ions can reach: $K = \frac{AT}{Z^2}$, where A is an atomic mass of an ion and Z is atomic number of an ion. For a solar cell test the SPC1 in conjunction with SSC were used to deliver an alpha beam of 35MeV to the AFRODITE array with the solar cell array as shown in figure 3.2. The beam was tuned and focused on the middle of the target by the ruby, which was located under the solar cell array. Prior to the experiment the chamber was evacuated and operators in the control room confirmed the beam energy.

5.3 Solar cell array

Due to a shortage of electronics for AFRODITE, individual solar cells were soldered together (3 or 2 per channel) to form 18 channels. This allowed only half of the LEPS and half of the clovers to be connected into clover electronics channels, while the LEPS electronics channels were used for the solar cell array. Figure 5.1 shows how the individual solar cells of the array were wired together to form 18 channels, while table 5.1 shows channels and the corresponding number of the solar cells. Two cells formed the channel number 5 and 11 for beam entrance, and beam exit, and channel 2 had two cells because of the target holder. The wiring was done with small shielded connectors to avoid interference.

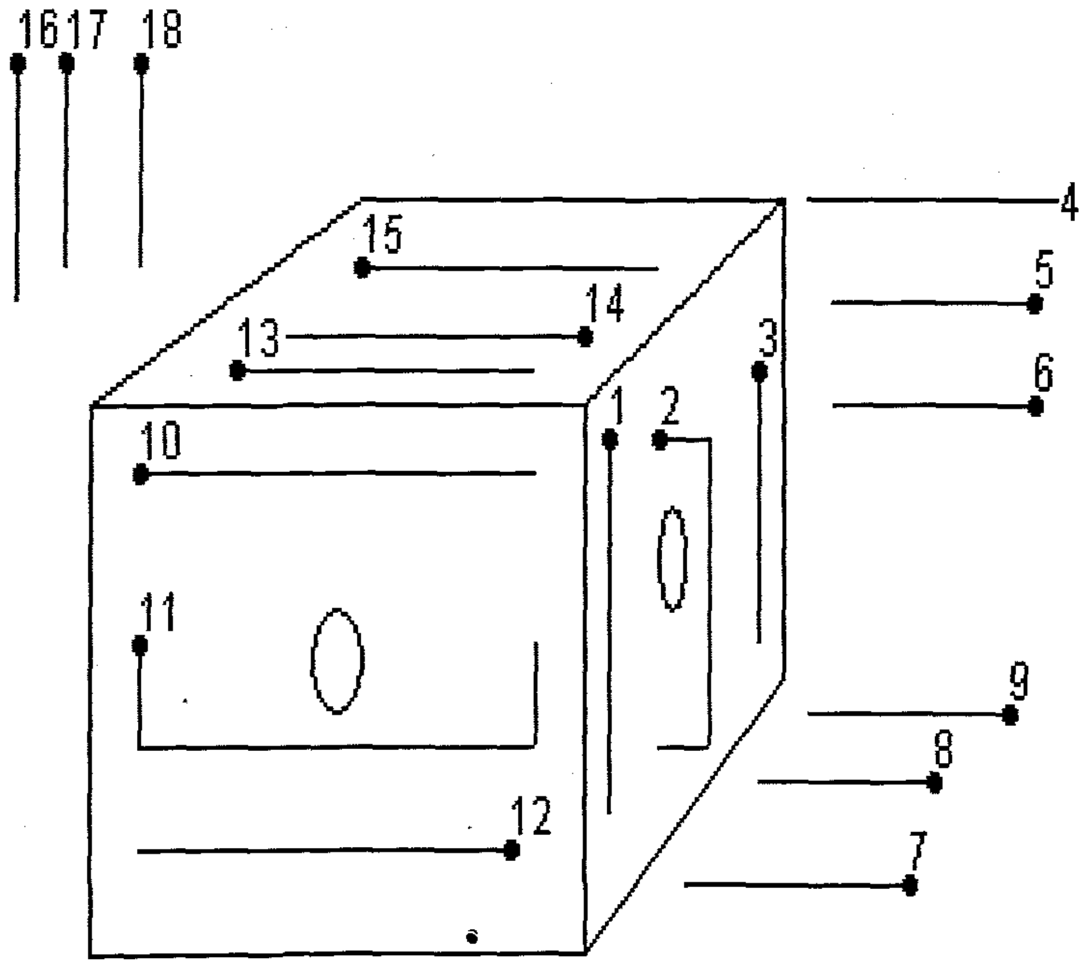

Figure 5-1: The illustration of the solar cell array with channels.

Channel number	Number of solar cells
1	3
2	2
3	3
4	3
5	2
6	3
7	3
8	3
9	3
10	3
11	2
12	3
13	3
14	3
15	3
16	3
17	3
18	3

Table 5.1: The channels as well number of solar cells soldered per channel.

CHAPTER 6 THE EXPERIMENTAL SETUP

The experimental setup of the electronics for the solar cell test experiment was similar to the setup of the AFRODITE except that the three LEPS and four Clovers that were used had their signals processed in clover modules, and the LEPS electronics were used to process the signals from the solar cell array.

6.1 Electronics

A block diagram of the AFRODITE electronics is shown in figure 6.1. The signals from the solar cells were fed into the preamp and then amplified by CAEN N568 amplifiers, which amplify and shape the 18 solar cells signals into a fast and linear signals. The fast signals were then fed into a Constant-Fraction Discriminator (CFD), which changes the analog input into a logic form, which is then fed into both a fan-in module and Gate and Delay Generator (G&DG). The G&DG delays the individual solar cell signals until the start signal of the TDC (where the solar cell times are measured) arrives, while the fan-in accepts the signals from the 18 channels of the solar cell array and gives the ORed output. The ORed solar cell signals are fed into the multiplicity unit, which give a selectable logic output depending on the number or multiplicity of inputs that have fired. The Multiplicity unit is normally used by the LEPS detectors. In this experiment, only one input was used, corresponding to the OR of the solar cell array. A choice could then be made; selecting a multiplicity of one would force the solar cell into the trigger. In practice a multiplicity of zero was chosen, meaning that data were recorded whether or not the solar cell array had fired, so that the efficiency could be assessed offline.

The RIS modules performed the signal processing for the 4-clovers and 3-LEPs in this experiment. This module has an integrated circuit that performs the same function as the electronics described for the solar cells. It includes the standard fast-slow processing shown in figure 6.2 and it also performs the antiCompton veto of events as shown in figure 6.3. The clean Ge signals indicating that a clover or a LEP had fired without the detection of a Compton scattered gamma ray by a BGO, are fed into a coincidence unit which was set to dual coincidence i.e. the trigger required that two detectors (Clover or LEPS) had fired. The output of both multiplicity units was then ANDed in the 365 AL coincidence units to form the trigger.

Once the trigger was generated, it was fanned out to the various ADC's and TDC's and the RIS modules. One branch gated the Silena 4418/V ADC's, which digitalized the solar cell energies. Another branch enabled the digitization of energy and time in the RIS module by gating the clean Ge signal of the RIS module back into itself, into its trigger 1 input, which tells the module to commence conversion.

To complete the process, one branch of the trigger fan-out was used to create an RF-gated trigger, which is used as the time reference and gate for various TDCs. A sample of the timing diagram is shown in figure 6.4. The reference is the cyclotron time. In this experiment, the pulse separation was 266.7 ns. When two clean Ge signals arrive at the coincidence unit (Ge1 and Ge2) the trigger signal is generated for the duration when both logic signals are true. In figure 6.4, the Ge2 is delayed as compared to Ge1 and a delayed trigger is generated as B (see figure 6.1). The trigger is then stretched by the G&DG to produce signal C, which is then ANDed with the RF to produce the signal at D (RF gated Trigger).

The RF gated trigger is fanned out to the LEPS TDC (4418/T) where it is then fed to the common start, which starts the time measurement in the TDC. The logic signals from the LEPS are delayed so as to arrive after common start and each signal stops the TDC allowing the time to be measured. The RIS modules also have internal TDCs that instead use the common stop mode. The RF-gated trigger is used as the common stop, by applying it to the trigger 2 input after a suitable delay. The RIS module TDCs and ADCs are read out on the FERA bus by a VME module, the F2VB, and thereafter the data are sent to a LINUX PC, which writes the data to the tape. During the readout, the 365 AL coincidence unit, where the trigger is generated, is vetoed to prevent acquisition until the system is ready to accept another event.

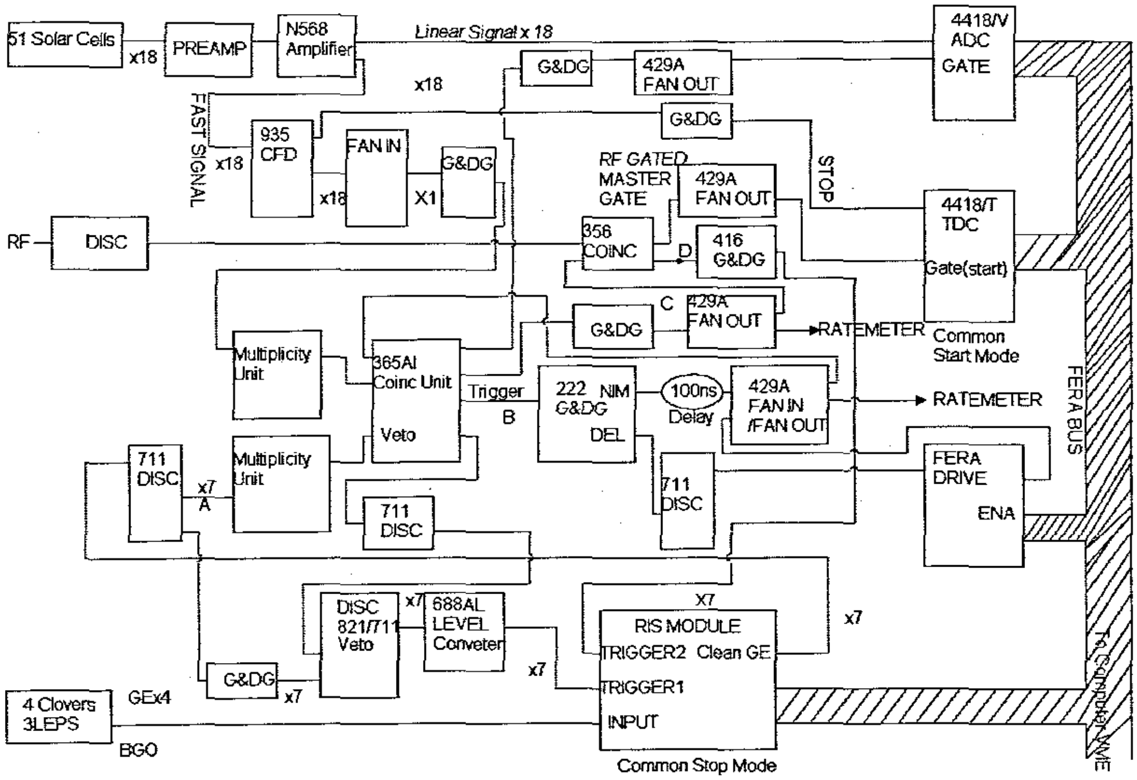

Figure 6-1: The electronics setup of a solar cell array test experiment.

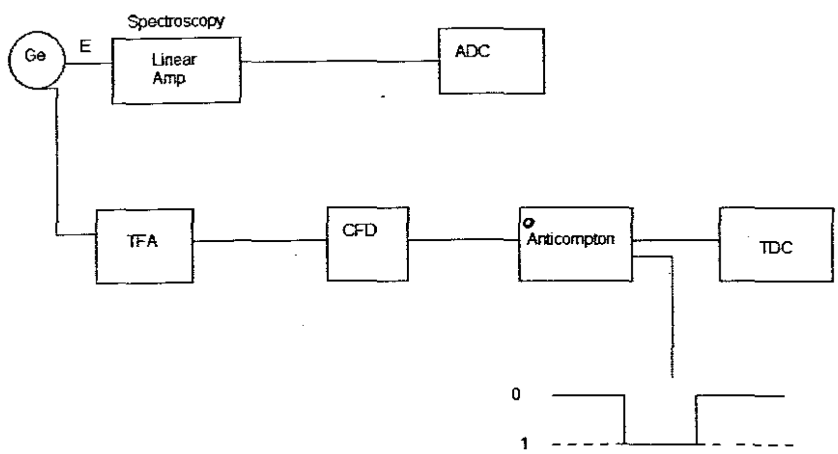

Figure 6-2: Parts of the electronics that takes place in the RIS modules.

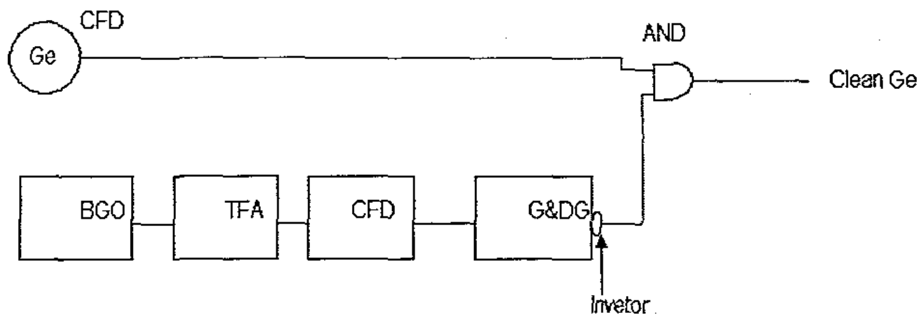

Figure 6-3: The antiCompton electronics process that takes place in the RIS module.

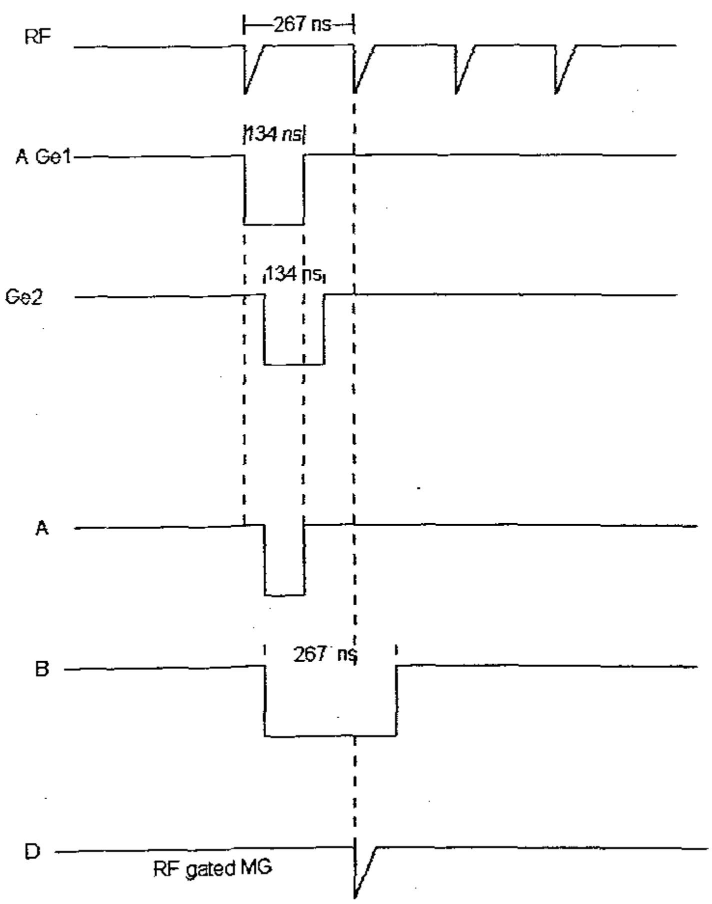

Figure 6-4: The RF time signal coincident with the Germanium time signal see figure 6.1.

6.2 Online Spectra

MIDAS software in the data room was used to observe online spectra and to manage the data collection. Therefore, this section presents the spectra that were observed online.

The online solar cell energy spectra from the $^{232}Th + \alpha$ reaction taken at different angles with respect to the beam axis are shown in figure 6.5. The corresponding time spectrum is shown in figure 6.6. The broad peaks around channels 200 and 600 in the solar cell energy spectra (see figure 6.5) were proved to be from fission by swapping the ^{232}Th target with a ^{152}Sm target, from which there was negligible fission. The online solar cell energy spectrum from $^{152}Sm+^{4}He$ reaction is shown in figure 6.7, where only low energy noise is present.

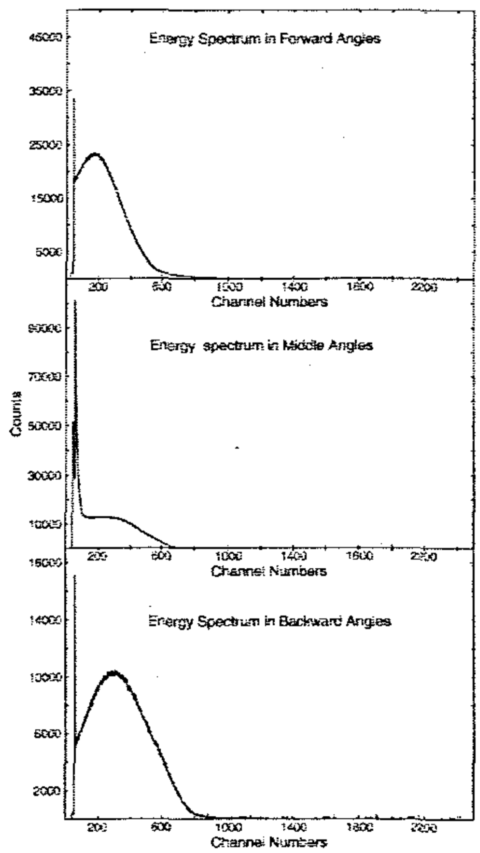

Figure 6-5: The solar cell energy spectra observed in forward, middle and backward angles during $^{232}Th+^{4}He$ reaction.

The fission fragments detected in the middle-angles solar cells (see figure 6.5) are reduced in energy due to the greater effective target thickness and shadowing by the target frame. The time spectra for all angles were similar to the one presented in figure 6.6.

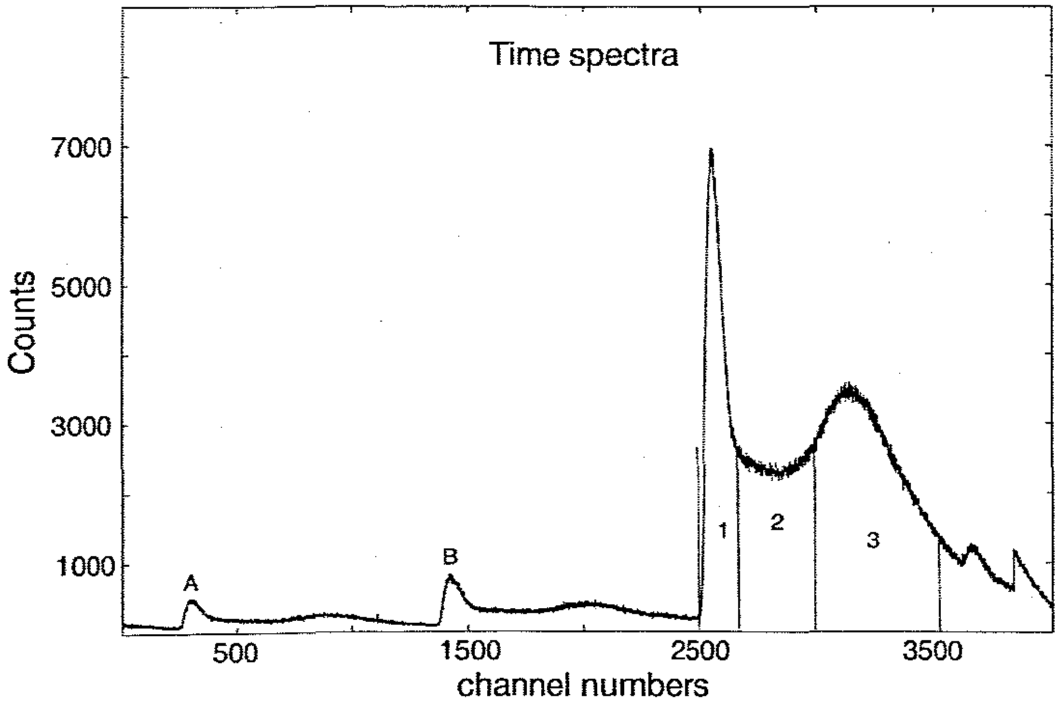

Figure 6-6: The solar cell time spectrum observed during $^{4}He+^{232}Th$ reaction.

The large peak in the solar cell time spectrum (see figure 6.6) that is separated into regions 1, 2 and 3 was thought to be from fission fragments and alphas emitted, and the smaller peaks labelled A and B were due to random coincidence from earlier beam pulses.

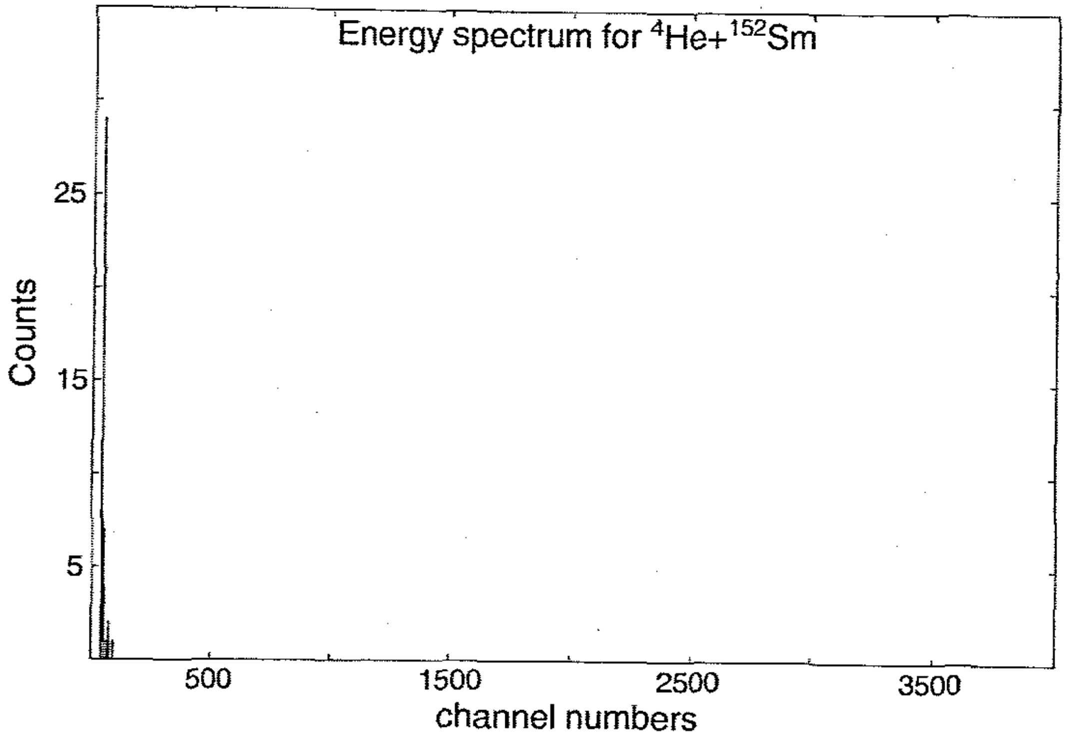

Figure 6-7: The solar cell energy spectrum during $^{4}He+^{152}Sm$ reaction.

The online clover energy spectrum observed (from only one detector) is shown in figure 6.8 and it time spectrum is shown in figure 6.9. The large radiation background from the clover spectrum for example peak 200 keV etc, were thought to be due to the reaction of an alpha with the beam at the entrance to a solar cell array.

The largest peak in the clover time spectrum (see figure 6.9) is the prompt beam-related peak, and the smaller peaks on the left hand side of the largest peak correspond to later beam pulses, while those on the right hand side correspond to the earlier beam pulses because the RIS module TDC operates in common stop mode. The difference in time between two pulses is known from the RF frequency. The LEPS time spectra were similar to clover time spectra since they too were generated from clover modules. The LEPS energy spectrum observed during ^{4}He+^{232}Th reaction is shown in figure 6.10.

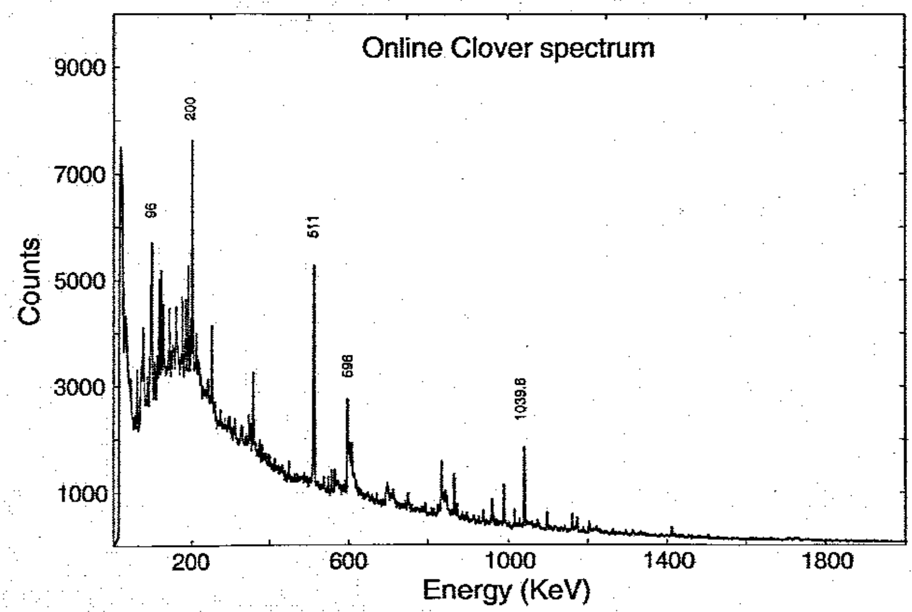

Figure 6-8: The clover energy spectrum observed during ^4He+^{232}Th.

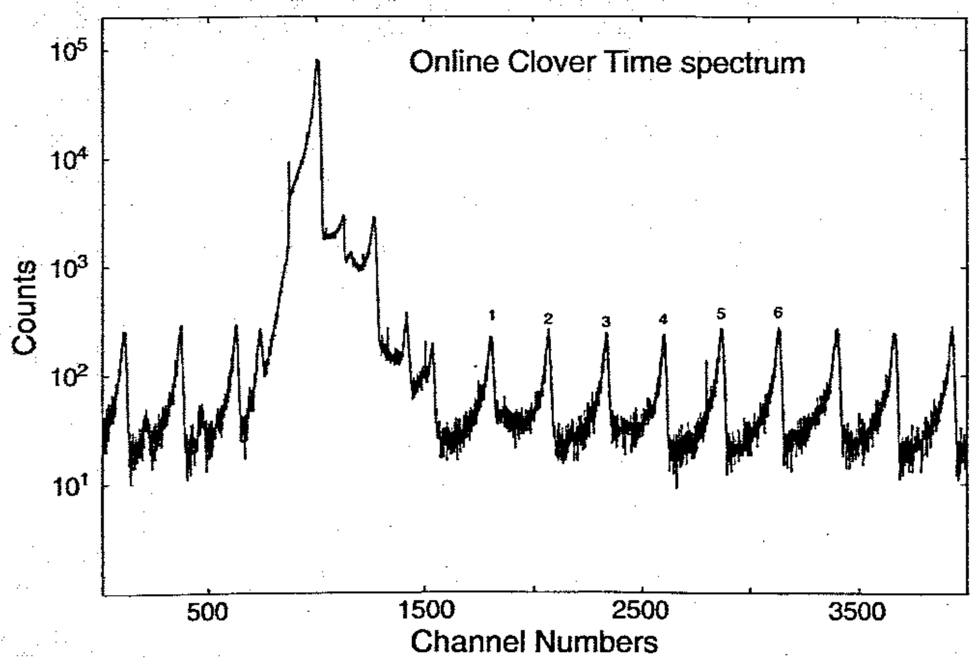

Figure 6-9: The clover time spectrum observed during ^4He+^{232}Th reaction.

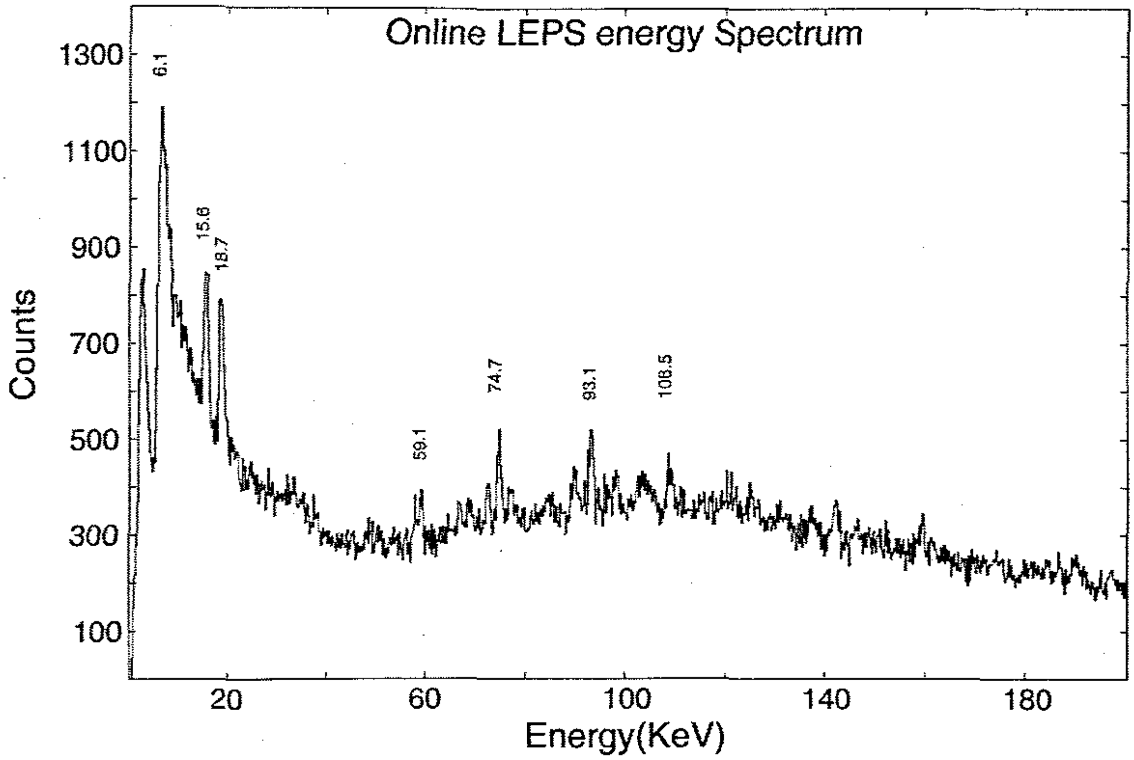

Figure 6-10: The LEPS energy spectrum observed during ^{4}He+^{232}Th reaction.

CHAPTER 7 RESULTS AND DATA ANALYSIS

The data for the solar cell test experiment (α + ^{232}Th at 35 MeV) were stored onto a Digital Linear Tape. At the end of the solar cell test experiment, the data were copied to a disk. This chapter discusses the offline data analysis and the results for solar cell test experiment.

7.1 Calibration of Detectors

The data for the energy calibration of the detectors (LEPS and Clovers) was taken at the end of the last run of the solar cell test experiment by placing ^{152}Eu and ^{133}Ba sources at the target position. The peak positions of both sources were then determined using the SFIT program. This program finds peak positions automatically and those that it failed to find were then found by using the GF3 program. The GF3 program allows the user to fit the peak manually thus finding its position. The peak positions were then fed to the SCAL program, which fits an energy calibration to each detector of the form $E = a_0 + a_1 x + a_2 x^2$, where x is the channel number. Then the program called DOP_COR was used to produce the gain matching coefficients, which maps the channels to calibrations of $E = 0.2x'\,\text{keV}$ and $E = 0.5x'\,\text{keV}$, where x' are the new channels, for LEPS and clovers respectively. The LEPS were calibrated using ^{133}Ba, while ^{152}Eu was used for the clovers

7.2 Time calibration

The desire to make all the prompt time peaks for both clovers and LEPS appear at the same channel number i.e. channel 1000, required a time calibration and time gain matching. This was done by finding the peak position of the time spectra using the GF3 program, and finding the separation of six pulses (see figure 6.9) in terms of channel numbers, since the separation in terms of time was known from the RF frequency. The separation of five successive beam pulses in terms of channel numbers and in terms of time were used to calculate the gradient, *m*, in channels/seconds units. The separation between five beam pulses was 1333.5 ns in this experiment. The times were matched to 1 ns per channel, with the prompt at channel 1000, i.e.

$t = mx_0 + C$

where m is the slope and C is the constant, which was calculated using $C=1000-mx_0$, where x_0 is the centroid of the prompt peak (see figure 6.9), assumed to arrive at time $t_0= 1000\ ns$.

7.3 Gamma-rays From Fission Fragments

The sorting software called MIDAS was used to sort the data. This software allows one to write the programs for sorting data using the MTsort Language.

Since one region in the solar time spectra (figure 6.6) could have corresponded to alpha particles and another to fission fragments. The first step that was taken, as an attempt of finding the gamma rays from fission fragments, was to try to find the regions that correspond to fission fragments in the solar cell time spectrum (see figure 6.6) and then use them and their solar cell energy spectra to find the gamma rays from fission fragments. As an attempt of finding which region corresponds to fission fragments, gates were set on these regions (1, 2, and 3) and the solar cell energy spectra corresponding to these regions were incremented per region. The solar cell energy spectra obtained by setting gates in these three regions are shown in figure 7.1. The obtained solar energy spectra indicated that the three regions were from fission fragments because the obtained solar cell spectra were having the shapes similar to that of the original solar cell energy spectra (ungated spectra in figure 7.1). That proved that these regions (1,2&3) could be used in getting gamma rays from the fission fragments. In other words, the peak that is formed by regions 1,2 and 3 belongs to fission fragments not alphas that are scattered. It is possible that the strange shape of the solar cell time is due to the charge collection process in the solar cell or to the incorrectly adjusted CFDs.

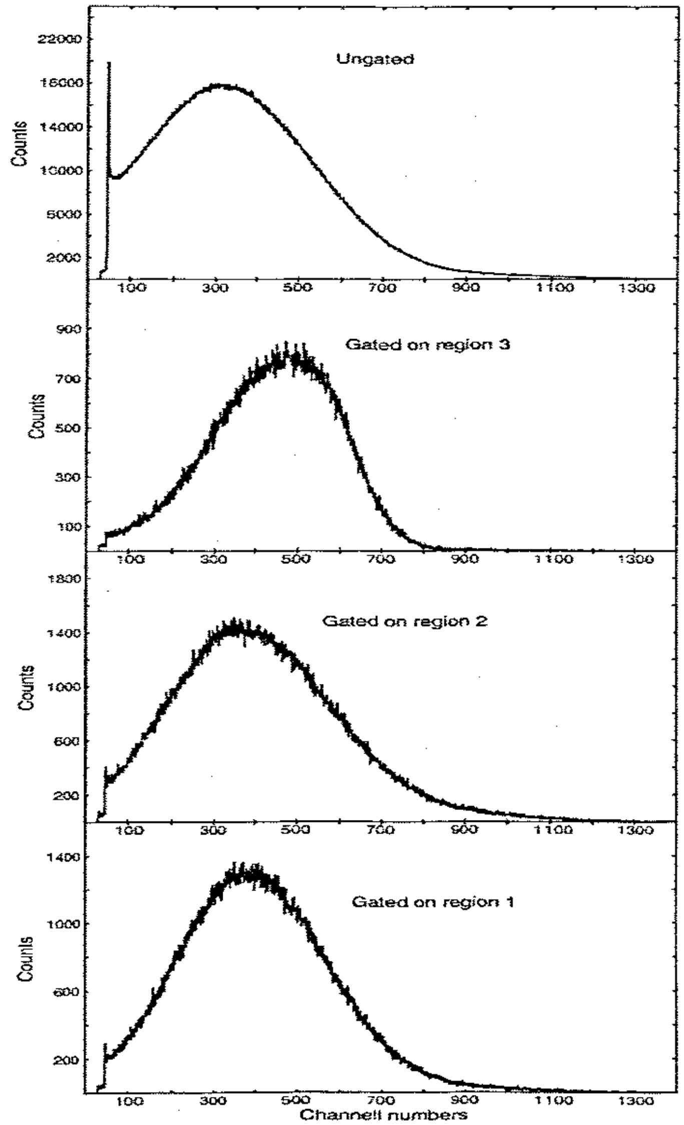

Figure 7-1: The projection of solar cell energy spectra, the first from bottom to top, is when gated on region 1, is when gated on region 2 and is when gated on middle region and is ungated solar cell energy spectrum.

Prior to the process of finding gamma rays from the fission fragments, the MTSort sorting software was used to sum the gamma spectra from the four clovers and three LEPS. The total Clover spectrum produced is shown in figure 7.2 and total LEPS spectrum is shown in figure 7.3, they are similar to online spectra for individual detectors but of course have better statistics.

In order to find gamma rays from fission fragments, the gates were set on time (regions 1,2 and 3, see figure 6.6) and on the solar cell energy spectra of the solar cell array (such that the fission fragments energy peak (broad peak around channels 200 to 600) is the only peak inside gate), the total gamma-ray spectrum was incremented when ever those gates were valid. This was done when 0 solar cells fired, 1 solar cell fired and when 2 solar cells fired. The corresponding spectra obtained are shown in figure 7.4. The spectra obtained by gating on solar cell time and energy when 1 solar cell fires or 2 solar cells fire were similar as seen in figure 7.4, but the difference in statistics was quite large.

The gamma rays obtained through this process were believed to be associated with fission fragments because some of the gamma peaks in the spectra obtained when 0 solar cell fires disappeared when one solar cell fires or two solar cells fire. For example, in figure 6.5, 200.4keV and 358.5 disappear, when 1 solar cell or 2 solar cells fire, which suggests that the remaining gamma rays are associated with fission.

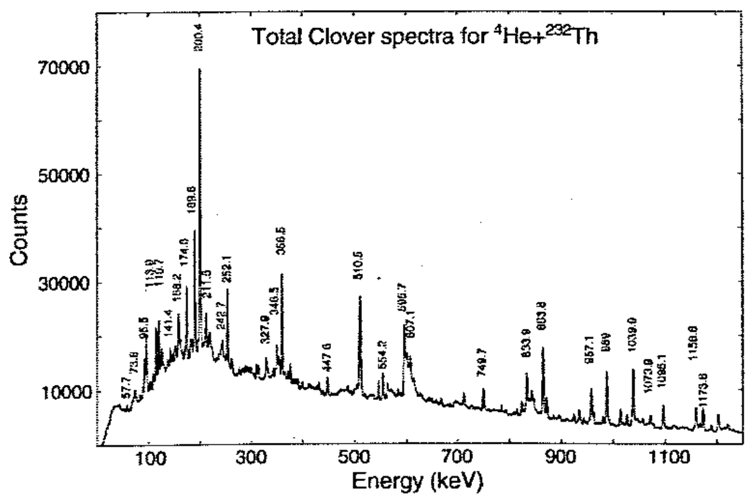

Figure 7-2: The total gamma spectra for Clovers.

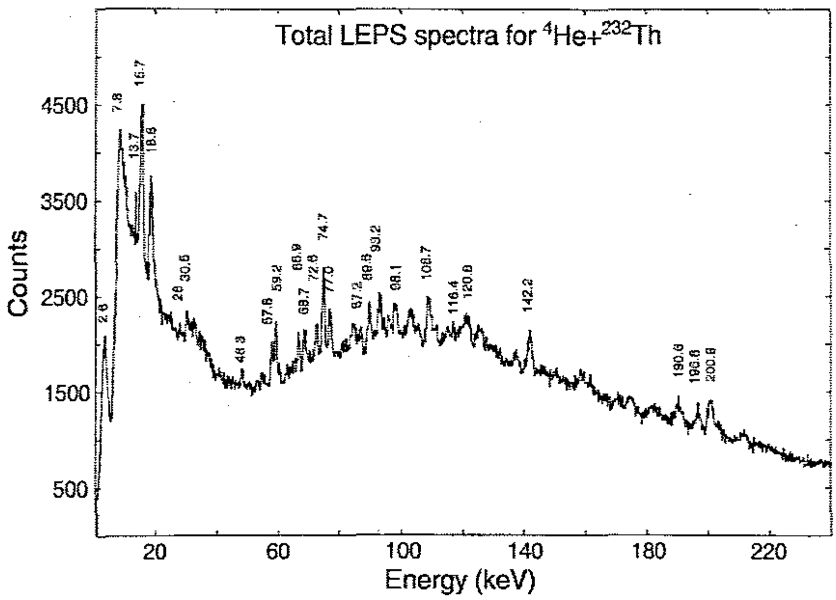

Figure 7-3: The total gamma spectra for LEPS.

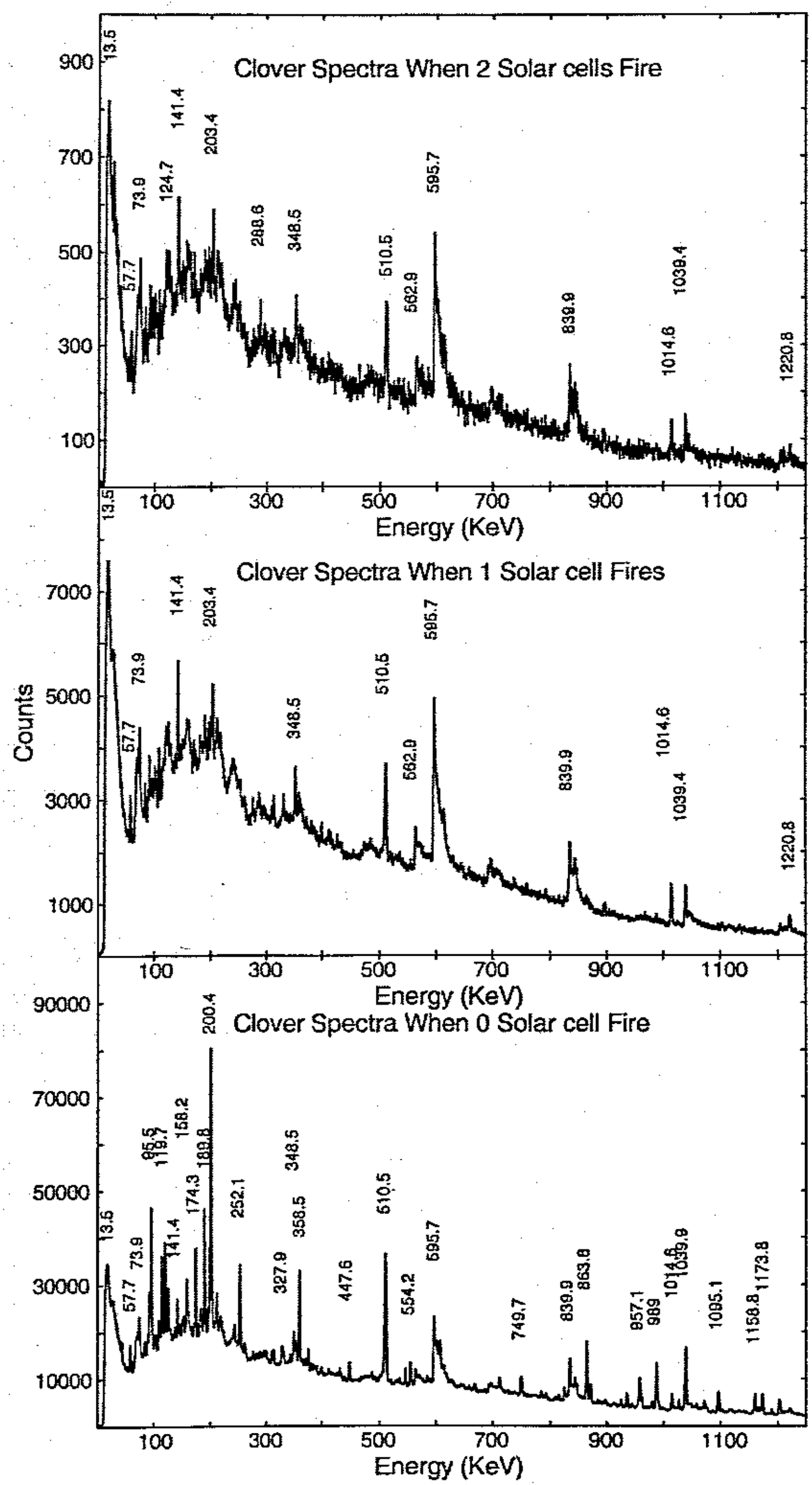

Figure 7-4: The total gamma spectra, top when 2 solar cells fire, middle 1 solar cell fire and bottom 0 solar cell fire.

7.4 Attempt to Identify Gamma-rays associated with fission.

During the fission process, fission fragments and also neutrons are emitted. The gamma rays that are expected are the ones emitted when the neutrons interact with the germanium detector, the others from the fission fragments. Fission fragments can either emit gamma rays when they are in flight or when they are stopped in the solar cell. The gamma rays emitted in flight are expected to be Doppler shifted.

As an attempt to identify the gamma rays associated with fission, a gamma-gamma clover coincidence matrix when either one or two solar cells fired was created. This was done so as to find all coincidence gamma rays, which would allow one to build the level scheme of the nucleus. The projection of such matrix was similar to gamma spectra in figure 7.4(when 1 solar cell fires and 2 solar cells fire). There are only three peaks that have been identified in the gamma spectra namely 595.7, 839.9 and 1039.9, which have been found to be due to the gamma rays emitted when a neutron interacts with germanium. The gamma rays from gamma-gamma matrix have not been identified due to the following factors: the nucleus fission into many different fission fragment species; the low statistics in the gamma-gamma matrix; the Doppler shift has not been corrected in this experiment for those gamma rays that are emitted in flight.

7.5 The Efficiency of Solar Cell Array

Since no gamma rays lines from a specific fission fragment could be identified, the efficiency was calculated using the ratio of counts (*R*) when 1 solar cell fired to 2 solar cells fired. Taking the probability of detecting a fission fragment to be ε, which is equivalent to the efficiency of the solar cell array, that of not detecting a fission fragment is $1-\varepsilon$. Therefore, the probability of detecting one out of two fragments is $2\varepsilon(\varepsilon-1)$ i.e. it can be fission fragment number 1 or number 2. The probability of detecting both fragments is ε^2. Then the ratio of counts, R, in the spectrum obtained when two solar cells fire to the one when at least one solar cell fires is:

$$R = \frac{\varepsilon^2}{\varepsilon^2 + 2\varepsilon(1-\varepsilon)},$$

when solved for the efficiency ε gives:

$$\varepsilon = \frac{2R}{1+R} \qquad 7.1$$

R was found by first finding the total counts of both spectra using GF3. The counts in the spectra were 5052776(single solar cell fired) and 547033(two solar cell fired), which gave a ratio, *R*, of 0.1083. Using equation 7.1, the efficiency (ε) of 0.195376 was obtained, equivalent to 20%.

This efficiency is for 30 solar cells, since it was found by checking the solar cell spectra with MIDAS that only 30 out of 51 cells in the array had both energy and time working, due to loose cables and dead channels on various modular electronics. To find the expected efficiency if all solar cells in the array were working, the efficiency of the solar cell array of 20% was multiplied by 51/30, (20%x51/30), which implies that if all the solar cells worked, the efficiency would be of about 34%. If one compares the geometric efficiency (74%) with the expected detection efficiency (34%), one may see that almost 40% is missing. The lost efficiency may be due to the stopping of fission fragments in the target, shadowing by the target frame and losses in data collection process due to the electronics.

The efficiency loss of fission fragments in the target and frame shadowing, can be calculated from knowing the target thickness, the dimensions of the frame and the angular distribution of the fission fragments at different angles along the beam. There are two relevant angles for this calculation. Firstly, there is θ_1, the minimum angle between the line perpendicular to the beam's path and the trajectory thickness at which the fission fragments could lose enough energy to fall below the CFD threshold and not detected. Secondly there is θ_2, the angle defined by the target frame i.e. the maximum angle between the line perpendicular to the beam's path and the edge of the target frame.

These two angles in our case can be seen in figure 7.5, where dimensions of the frame and the target are also shown. Angle θ_1= 1 (for the loss of fission fragments) in figure 7.5, is the one between the vertical dotted line and the line 4.5 mgcm^{-2} labelled by angle θ_2 =2 (for frame shadowing) is between the vertical dotted line and the line to the Al frame edge.

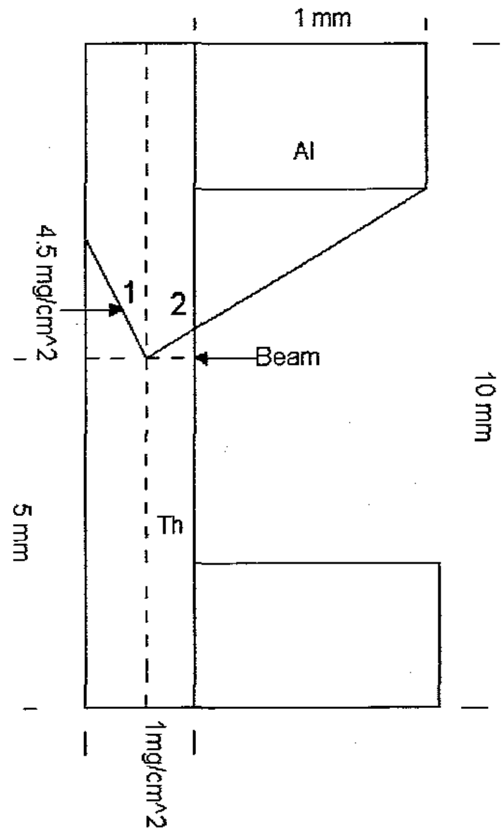

Figure 7-5: The illustration of target and frame dimensions for the efficiency loss due to the stopping of fission fragments in the target and due to shadowing by the frame (Al)(angle 1=θ_1 and angle 2=θ_2).

The thickness 4.5 $mgcm^{-2}$ is that at which the fission fragments would lose all their energy and fall below the CFD threshold. This thickness was calculated by first assuming ^{132}Sn to be the fission fragment of 100 MeV and a threshold of 40 MeV. Then the STROP3 program (this program uses the Zielgler stopping powers to estimate thickness or energy loss [Zie77]) was used to calculate the thickness that would stop the fission fragments, which was found to be 4.5 $mgcm^{-2}$. Using the dimensions in figure 7.5, θ_1 and θ_2 were found to be 6.3° and 11° respectively, and then the angles with respect to beam axis were found to be 83.7° and 101° respectively.

The angular distribution of fission fragments measured by Coffin et al and Endt et al show that the fission fragments tend to come off forward and backward along the beam axis. The measured values of anisotropies for fission fragments for Uranium is 1.5 on forward and backward angles along the beam path and is 1 at 90° [Cof58][End62]. Such an angular distribution is demonstrated in figure 7.6, and can be represented by $W(\theta) = \frac{3}{2} - \frac{1}{2}\sin(\theta)$.

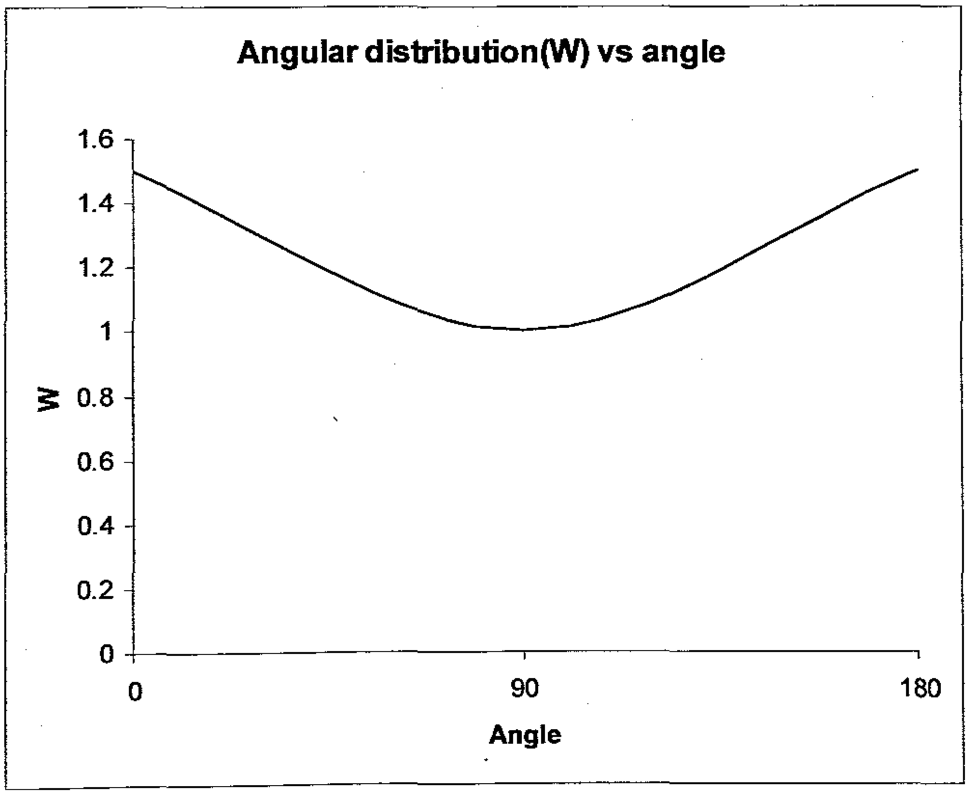

Figure 7-6: The fission fragments angular distribution as a function of angles along the beam [Cof58] [End62].

To calculate the lost efficiency, the area under the distribution curve (figure 7.6) was found together with one corresponding to the losses from the effects discussed above. The ratio of the area corresponding to the losses (area from 83.7° to 101° with respect to beam axis) to the area under of angular distribution curve of fission fragments for

0° to 180° was found to be 0.096. Hence ~10% of efficiency was lost. Therefore, out of the total of 40% lost efficiency 10% is due to shadowing and loss in the target, and the other 30% is presumably due to losses in the by data collection process due to inefficiency in the electronics.

CHAPTER 8 SUMMARY AND FUTURE STUDIES

The aim of this study was to develop the fission suppression devices for AFRODITE at iThemba LABS (South Africa). These two fission suppression devices are the recoil detector and the solar cell array.

The recoil detector has been tested with a ^{252}Cf fission source and found to work but with some problems. For example, the feed throughs broke down at high voltage (~1500V) and there was ringing on the output signal. Due to the late arrival of the new feed throughs, the recoil detector has not been tested in-beam, whereas, the solar cell array has been tested with the ^{232}Th (α, xn)^{233}U reaction. Its corrected efficiency has been found to be 34%, which was half of the calculated geometric efficiency of about 74%. Approximately 10% of the lost efficiency has been found to be due to frame shadowing and the loss of fission fragments in the target, while the other 30% is probably to be due to dead time in the electronics. The reduced efficiency is only useful for the study of the gamma spectroscopy in the first minimum.

Further studies are necessary in order to fully understand the unusual shape of solar cell array time spectra, to understand the reduction in efficiency from that expected and the test of the recoil detector should be done so as to find its efficiency in order to compare with the solar cell array.

APPENDIX

Derivations of some of the Hands Equations for Recoil Detector parameters

For particle of mass *m*, with charge *q* and speed *v* moving perpendicular to uniform magnetic field *B*, on a circular orbit with radius of curvature ρ, the Lorenz force is equal to centrifugal force:

$$qvB = \frac{mv^2}{\rho}$$

$$\rho = \frac{mv}{qB}$$

$$from$$

$$P = mv$$

$$p = qB\rho$$

The equation relating the total energy E of a particle and the momentum *p* of a particle is:

$$E^2 = p^2c^2 + mc^2$$

Where $E = E_0 + E_k$ and $E = mc^2$

With E_0 = the rest energy of a particle

E_k = the kinetic energy of a particle

c = speed of light

$$\therefore B\rho = \frac{c^2 mv}{c^2 q}$$

$$B\rho = \frac{E\beta}{qc}$$

Where $\beta = v/c$ and with $\gamma = E/E_0$ where $\gamma = \frac{1}{\sqrt{1-\beta^2}}$

$$B\rho = \frac{E\sqrt{1-\gamma^2}}{qc\gamma}$$
$$Bp = \frac{\sqrt{E^2 - E_0^2}}{qc}$$
$$B\rho = \frac{\sqrt{E_k^2 + 2E_0E_k}}{qc}$$
$$B\rho = \frac{\sqrt{E_k^2 + 2E_0E_k}}{Qc}$$

If a voltage is applied in an electron with charge e, the work done by the voltage is:

$$W = eEs.................1$$
$$W = \frac{eVs}{s}..................2$$
$$W = eV.......................3$$
$$W = \Delta U = \Delta K..............4$$
$$\therefore \frac{1m_e v^2}{2} = eV.................5$$
$$v = \sqrt{\frac{2eV}{m_e}}..........................6$$
$$v = 592.694 \times 10^3 \sqrt{V}(m/s).........7$$
$$v = 592.694 \times 10^3 \times 10^6 \times 10^2 \times 10^{-9} \sqrt{V}(cm/ns).....8$$
$$v = 59.2694 \times 10^{-3} \sqrt{V}(cm/ns)........................9$$

The radius of curvature *(r)* in a uniform magnetic field (*B*):

$$F_B = F_C$$
$$ev \times B = \frac{mv^2}{r}$$
$$evB = \frac{mv^2}{r}$$
$$eB = \frac{mv}{r}$$
$$rB = \frac{mv}{e}$$
$$rB = 3.374 \times 10^{-6} \sqrt{V}(from(9)in(Tm))$$
$$\therefore rB = 3.374 \sqrt{V}(in(Gcm)$$
$$\therefore r = \frac{3.374\sqrt{V}}{B}$$

Time of flight (*t*) over distance (*d*) in field-free region after acceleration by a voltage (*V*):

$$v = 59.2694 \times 10^{-3}\sqrt{V}$$

$$t = \frac{d}{v}$$

$$t = \frac{16.87d}{\sqrt{V}}$$

Time of flight (t) for 180° bend:

$$v = 59.2694 \times 10^{-3}\sqrt{V}$$

$$d = \pi r = \pi \times \frac{3.374\sqrt{V}}{B} = \frac{10.5997\sqrt{V}}{B}$$

$$\therefore t = \frac{10.5997\sqrt{V}}{B} \times \frac{1}{59.2694 \times 10^{-3}\sqrt{V}}$$

$$t = \frac{178.849}{B}$$

$$t = \frac{179}{B}$$

Time of flight when starting from rest in a uniform electric field (*E*=*V*/*d*):

$$F = qE$$

$$F = eE$$

$$m_e a = eE$$

$$a = \frac{eE}{m_e}$$

by

$$d = \frac{1at^2}{2}$$

$$t = \sqrt{\frac{2d}{a}}$$

$$t = \sqrt{\frac{2d^2 m_e}{eV}} = \sqrt{\frac{2 \times 9.11 \times 10^{-31}}{1.6 \times 10^{-19}}}\frac{d}{\sqrt{V}}$$

$$t = 33.7\frac{d}{\sqrt{V}}$$

REFERENCES

[Ahm95] I.Ahmad and W. R. Phillips, Gamma rays from Fission Fragmens Rep.Prog.Phys.**58** (1995) 1415-1463

[Bec94] J. A. Becker, K. H. Maier, P. Fallon, A. O. Macchiavelii, J.A. Cizewski, C.J. Lister, E. F. Moore, A Recoil Fragments Filter for GAMMASPHERE, **1994**

[Blo89] J. Blons, Nucl.Phys.**A502** (1989) 121c

[Bra00] P. D. Bradley, PhD Thesis, University of Wollongong, **2000**

[Bru54] H. Bruining, secondary Electron Emission. Pergamon Press, New York. **1954**

[Cle73] H-G. Clerc, H. J. Gehrhardt, L. Richter and K. H. Schmidt N.I.M. **113**(1973) 325

[Cof58] C. T. Coffin and I. Halpern, Angular Distribution in Fission Induced by Alpha Particles, Deutrons, and Protons, Physical Review, **Vol 112,** number 2(1958) 536-543

[Cwi94] S.Cwiok, W. Nazarewicz, J. X. Saladin, W. Ploceinnik and A. Johnson, Hyperdeformations and clustering in actinide nuclei, Phys. Lett. **B322** (1994) 304

[Duc99] G. Duchene et al, N.I.M.in Phys.Res.**A432** (1999) 90

[End62] P.M. Endt and P.B. Smith, Nuclear reactions, Vol ii, contributors, S. D. Bloom et al, North-Holland Publishing Company-Amsterdam, **(1962)** 42-112

[Has92] D. Hasselkeamp, H. Rothard, K. –O. Groeneveld, J. Kemmler, P. Varga, H. Winter, Particle Induced Electron Emmission II, Springer Verlag, **123**(1992) 97-145

[Haw99] D. Hawcroft et al, Acta Thys. Pol. **B30** (1999) 798

[Her03] B. Herskind et al, Proc. Of Conf."Labyrinth in Nuclear structure"Crete, **2003**

[Hub05] H.Hubel, Search for Hyperdeformation, Acta Phys, Pol. **B36** (2005) 1015

[Jon95] P. M. Jones et al, N.I.M.in Phys.Res. **A362** (1995) 556

[Kra98] A. Krasznahorkay et al, Phys.Rev.Lett. **80** (1998) 2073

[Lam01] M.J. Lamey, Masters Thesis, Simon Fraser University, **2001**

[Lar69] N. L. Lark et al, Spontaneously fissioning isomers in U, Np, Pu and Am isotopes, Nuclear physics **A139** (1969) 481-500; © North-Holland Publishing Co., Amsterdam.

[Lei95] M.Leino, N.I.M., **B99** (1995) 653

[Lei97] M.Leino, N.I.M., **B99** (1997) 320

[Lia88] E. Liatard, S. Akrouf, J. L. Bruandet, A. Fontenille, F. Glasser, P. Stassi and Tsan Ung Chsn, N.I.M. **A267**(1988)231

[Mab03] G. K. Mabala, PhD Thesis, University of Cape town, **2003**

[Mcl82] F.B. Mclean, T. R. Oldham, Charge Funneling in n- and p- type Si substrate, IEEE, Trans on Nucl. Sience, Ns-29, **No.6** (1982) 2018

[New98] R. T. Newman, J.J. Lawrie, B. R. S. Babu, M. S. Fetea, S. V. Förtch, S. Naguleswran, J. V. Piltcher, D.A. Raave, C. Rigollet, J. F. Sharpey-Schafer, C. J. Stevens, F.D. Smit, G. F. Seyyn, C. V. Wikner, D.G. Aschman, R. Beetge, R. W. Fearick, G.K. mabala, S. Murray, D. G. Roux, W. Whittaker and N. J. Ncapayi, Proceeding of Balkan School on Nucl. Phys, September1-10, 1998, Istanbul-TURKEY, Balkan Phys. Lett. **182**(1998)

[Ring80] P. Ring and P. Schuck, The Nuclear Many Body Problem (**1980**) 5

[Sch80] J. Schou, Physical Review **B22**, no.5 (1980) 2141

[Tec94] Technical information, MCP Assembly, Hamamatsu, May **1994**

[Thi02] P.G. Thirolf et al, Progress in Particles and Nuclear Physics, **49**(2002) 325

[Twi86] P.J. Twin et al, Phys. Rev. Lett. **57** (1986) 811

[Wad02] R. Wadsworth and P. J. Nolan, The influence of microstructures on rotational motion in nuclei, Rep.Prog.Phys.**65** (2002) 1079-1118

[Wah01] H. Wahl, QuarkNet presentation, June **2001**

[War83] D. Ward et al, Nucl. Phys. **A406** (1983) 591

[Www1] http://www.phys.jyu.fi/research/gamma/publications/ptgthesis/node2

[Www2] http://www.lnl.infn.it/~prisma/clara_technical/node3.html

[Zel77] A.M. Zebelman et al, N.I.M. **141**(1977) 439

[Zei77] J. F. Ziegler, Stopping Powers and Ranges in All Elements, **Vol. 4**, (1977)